Adhesion forces of radioactive particles measured by the Aerodynamic Method–Validation with Atomic Force Microscopy and comparison with adhesion models

Samuel Peillon, Thomas Gelain, Mickaël Payet, Francois Gensdarmes, Christian Grisolia, Olivier Pluchery

Journal of Aerosol Science 165 (2022) 106037

Contents lists available at ScienceDirect

Journal of Aerosol Science

journal homepage: www.elsevier.com/locate/jaerosci

Adhesion forces of radioactive particles measured by the Aerodynamic Method–Validation with Atomic Force Microscopy and comparison with adhesion models

Samuel Peillon [a,*], Thomas Gélain [a], Mickaël Payet [b], François Gensdarmes [a], Christian Grisolia [b], Olivier Pluchery [c]

[a] Institut de Radioprotection et de Sûreté Nucléaire (IRSN), PSN-RES/SCA, BP 68, 91192, Gif-sur-Yvette, France
[b] CEA, IRFM, F-13108 Saint Paul lez Durance, France
[c] Sorbonne Université, Institut des Nanosciences de Paris, 4 place Jussieu, 75252 Paris, Cedex 05, France

ARTICLE INFO

Editor: Dr. Chris Hogan

Keywords:
Adhesion
Roughness
Tungsten
Tritium
AFM
Resuspension

ABSTRACT

Median adhesion forces of tritiated tungsten micro-particles deposited on a glass substrate were successfully determined using an aerodynamic method (AM) which is presented in this paper. The original aerodynamic device built for these experiments has been carefully characterized in terms of friction velocities allowing to quantify aerodynamic torque exerted on the particles and to deduce median adhesion forces thanks to a force balance approach. Using the same particle/surface systems (non-radioactive tungsten particles in contact with a glass substrate), distribution of adhesion forces were obtained using AFM for comparison with the AM. The results show a good agreement between the two techniques which allowed to validate the AM. Furthermore, a precise description of the root-mean square roughness (*rms*) distribution of the glass substrate made it possible to compare the experimental results with different analytical adhesion force models. Integrating the *rms* roughness distribution of the substrate into the model of Rabinovich et al. showed the best agreement with the present experiments capturing most of the adhesion forces of 10 μm to 18 μm diameter tungsten particles. Moreover, the method developed in this work made it possible to show that the electrostatic image force arising from the self-charging of tritiated tungsten particles has a negligible contribution in the adhesion of the particles for the studied configuration.

0. Introduction

Control and sampling of dust deposited on surfaces are topics of interest in many domains where contamination by micro-particles can present risks for processes, devices or be harmful for the workers or the public. For example, these type of control are common to assess soiling on photovoltaic panels (Figgis et al., 2017; Ilse et al., 2019; Sarver et al., 2013), presence of explosive residues on surfaces (Kottapalli & Novosselov, 2019) or indoor environment pollutants (Boor et al., 2013). It can also be encountered in pharmaceutical, microelectronic, spatial or nuclear industries, to name a few (Barth et al., 2013; Gradoń, 2009; Mikellides et al., 2020; Pecault et al., 2012; Petean & Aguiar, 2015). Regarding the latter area, special attention to the safety and operation of next-generation nuclear fusion facilities has emerged over the years. Indeed, large amount of metallic dusts (Grisolia et al., 2019; Krasheninnikov et al., 2011; Sharpe & Petti, 2002) will be generated by energetic plasma-surface interactions that can cause

* Corresponding author.
E-mail address: samuel.peillon@irsn.fr (S. Peillon).

https://doi.org/10.1016/j.jaerosci.2022.106037
Received 10 February 2022; Received in revised form 31 May 2022; Accepted 2 June 2022
Available online 10 June 2022

List of Symbols

Forces

F_{50}	Median adhesion force (N)
F_{adh}	Adhesion force (N)
F_c	Capillary force (N)
F_D	Aerodynamic drag force (N)
F_e	Electrostatic force (N)
F_g	Force of gravity (N)
F_{im}	Electrostatic image force (N)
F_L	Aerodynamic lift force (N)
F_{po}	Pull-off force (N)
F_{vdW}	Force of van der Waals (N)

Greek letters

α	Particle polarization correction factor
α_i	Ion–ion recombination coefficient ($m^3\,s^{-1}$)
β	Lattice parameter (m)
δ	Vertical deflection of a cantilever (m)
$\Delta\gamma$	Work of adhesion ($J\,m^{-2}$)
ϵ_0	Permittivity of vacuum ($F\,m^{-1}$)
η	Dynamic viscosity of the fluid (Pa s)
Γ	The Gamma function
γ	Surface energy of adhesion ($J\,m^{-2}$)
κ	Spring constant of a cantilever ($N\,m^{-1}$)
κ_m	Relative permittivity of the medium
κ_p	Relative permittivity of the particle
κ_s	Relative permittivity of the substrate
λ	Scale of the Weibull distribution
λ_s	Wavelength of surface roughness (m)
μ	Location parameter of the LN distribution
μ_T	Tabor's parameter
μ_-	Negative ion mobility at standard conditions ($m^2\,V^{-1}\,s^{-1}$)
ν	Kinematic viscosity of the fluid ($m^2\,s^{-1}$)
ω	Interaction energy (J)
ρ	density of the fluid ($kg\,m^{-3}$)
σ	Scale parameter of the LN distribution
τ	Shear stress (Pa)
υ	Poisson's ratio

Other symbols

$C_{D\|\|}$	Drag coefficient
KR	Resuspension fraction
A	Hamaker constant (J)
a	Lever arm (m)
a_{DMT}	Contact radius within DMT theory (m)
a_{JKR}	Contact radius within JKR theory (m)
D	Particle-surface distance (m)

significant erosion of the vacuum vessel (VV) plasma facing-components (PFCs) made from beryllium and tungsten. To assess the safety of nuclear installations and the relevance of the associated radiation protection measures, an important step consists in determining the source terms of contamination during normal operation and for different accidental scenarios (Taylor & Cortes, 2014). Assuming contamination is in the form of dust or aerosols, these source terms are calculated using airborne release fractions

D_p	Particle diameter (m)
D_{50}	Median particle diameter (m)
E	Young's modulus (Pa)
$E_{\max}$	Maximal energy of the radioactive element (eV)
f	Correction factor
I_β	Ion pair production constant (s^{-1})
J	Number of charge unit acquired by a particle
K	Composite Young's modulus (Pa)
k	Shape of the Weibull distribution
k_A	Scaling factor accounting for the asperity height
k_s	Static friction coefficient
m	Self-charging rate of a particle
m_p	Mass of the particle (kg)
N_-	Total concentration of negative ions (m^{-3})
n_-	Ion concentration produced by β-decays (m^{-3})
n_{b-}	Natural ion concentration (m^{-3})
Q	Electric charge of a particle (C)
R	Reduced radius (m)
r	Radius of asperity (m)
R_p	Radius of the particle (m)
R_p^+	Dimensionless radius of the particle
Re_p	Reynolds number of a particle
rms	Root mean square roughness (m)
$u_\star$	Friction velocity ($m\,s^{-1}$)
w_i	Mean energy required to form ion pairs in air (eV)
z_0	Minimal distance (m)
g	Standard gravity acceleration ($m\,s^{-2}$)

which relate the quantity of aerosol emitted to the initial quantity of dust involved, depending on the scenario. In order to carry out such calculations using robust numerical simulations (Gelain et al., 2020), it is necessary to first perform experimental studies to specify the physical parameters to use in the models. Among the most important parameters, the nature, size and shape of the dust must be assessed. Likewise, the nature and roughness of the surfaces on which this dust is deposited are important parameters to assess the physical forces that cause the detachment of the particles. Thus, as part of the safety studies related to the operation of fusion reactors, particular attention is given to the sampling and characterization of the dust produced in these machines (Balden et al., 2014; Baron-Wiechec et al., 2015; Rubel et al., 2018; Widdowson et al., 2013).

Among the techniques available for carrying out controls and samples of particles, the most widely used are surface washing, vacuuming, control smears, or sampling by adhesive pads. These techniques can be quickly implemented and are easy to use but suffer from certain weaknesses, the most important being that the forces applied to remove the particles remain unknown. In a recent study (Peillon et al., 2020) we have addressed these issues using an aerodynamic system working with calibrated air flows to perform consistent sampling of micrometer particles deposited on the inner-walls of a fusion reactor. The use of air flows has the advantage that it does not require mechanical action to loosen the particles and the efficiency of this technique can be equivalent or even superior to traditional smear techniques as shown recently by Kottapalli and Novosselov (2021). This study carried out in the WEST tokamak allowed to identify tungsten particles of spherical shape and micrometric sizes. Based on these results, we proposed a proxy tungsten powder in order to perform laboratory experiments. In particular, we have shown that these particles can acquire an electrical charge when they are labeled with tritium, the radioactive isotope of hydrogen used in fusion reactions. In fact, when a particle contains a radioactive element, an electrostatic self-charging phenomenon appears due to radioactive decay (Clement & Harrison, 1991; Yeh et al., 1976). The extent of this phenomenon depends on the radionuclide, the size and density of the particle and the environmental conditions (Gensdarmes et al., 2001; Kim et al., 2014). For large tritiated tungsten particles in vacuum, our group have shown that they can acquire several thousand electrostatic charges, thus showing an electrostatic contribution in their adhesion to surfaces. Concerning the study of the adhesion of tungsten particles on tungsten surfaces having roughness similar to the walls of a tokamak, we have carried out recently a detailed study by atomic force microscopy (AFM) (Peillon et al., 2019). It emerges from these measurements that the van der Waals forces are dominant in the adhesion of these particles but that their strength decreases rapidly when the roughness of the surface increases as it is commonly accepted in the literature (Beach et al., 2002; Cheng et al., 2002; Götzinger & Peukert, 2004; Jacobs et al., 2013; Rabinovich et al., 2000b). This is because the van der Waals forces act at very short distances, typically a few nanometers, and the roughness of a surface will therefore push the particle away from the bulk substrate, thus weakening the adhesion forces. In contrast, electrostatic forces are forces that act over greater

distances, from nanometers to micrometers, and their contribution to adhesion can become predominant in some cases (Chung et al., 2010; Kweon et al., 2015; Zhou et al., 2003). In particular, when a particle is electrically charged and deposited on a rough surface, a significant electrostatic image force can occur. In the case where the leakage of charges between the particle and the surface is reduced by the presence of an oxide layer (which acts as a dielectric barrier), in the present case WO_x, we have calculated with a Monte-Carlo method that the electrostatic image force could reach several tens of nanonewtons fairly quickly when tungsten particles have specific activities of $100\,MBq\,g^{-1}$ and are in a vacuum environment (Dougniaux et al., 2019; Peillon et al., 2020). To estimate the influence of these electrostatic effects due to radioactivity on the adhesion of tungsten particles, we propose in this paper an experimental work using an aerodynamic method (AM) to investigate the detachment of the radioactive particles. To validate the method, we first performed adhesion measurements with non-radioactive tungsten particles with both an Atomic force Microscope (AFM) and the AM and compared the median adhesion forces obtained. Indeed, performing an AFM study with radioactive particles needs high experimental efforts that are not achievable in our laboratory. On the other hand, the aerodynamic method has been used extensively to study particle adhesion as shown by Fillingham et al. (2019), Guingo and Minier (2008), Ibrahim et al. (2008), Soltani and Ahmadi (1994). Mention may also be made of Jiang et al. (2008) who used this technique to study the effect of substrate roughness on the adhesion while Matsusaka et al. (2015) studied the effect of the electric charge of particles deposited on metallic substrates in the presence of an external electric field. To increase the detachment efficiency of particles, the use of specific nozzles to produce high-speed air jets has been proposed by various authors. The geometry of the nozzle, distance and angle of the jet relative to the substrate where studied by Masuda et al. (1994), Otani et al. (1995), Ziskind et al. (2002). These studies have shown in particular that the detachment efficiency is optimal for small angles (15°–30°) between the surface and the exit nozzle. Thus, by carrying out a precise characterization of the air flows at the particle's location, it is possible to calculate the aerodynamic torque exerted on the particle and derive its adhesion force from the first principles (Brambilla et al., 2017; Fillingham et al., 2019; Ziskind et al., 1997).

In Section 1, we propose some theoretical reminders on the forces acting on a spherical particle deposited on a surface and exposed to shear flow. On this occasion analytical adhesion models used to analyze the AFM and the AM experimental results are introduced. Section 2 presents the methodology to carry out AFM measurements and to obtain the adhesion force distributions between tungsten micro-spheres and a glass substrate. A detailed description of the roughness of the glass surface on which the force measurements are made is also given. In Section 3, the aerodynamic method and the experimental protocols is described, from the making of the particle deposits to their analysis by optical microscopy. A discussion on the experimental results obtained is proposed in Section 4 with a comparison between the median adhesion forces measured by the two experimental techniques (AFM and AM) and various analytical adhesion models for the case of non-radioactive tungsten particles. Finally, we give the results obtained with radioactive tungsten particles labeled with tritium. A discussion on the influence of electrostatic image force due to radioactivity is proposed at the end of Section 4.

1. Theoretical considerations

A particle deposited on a surface and exposed to an air flow will experience attractive forces and detachment forces resulting from its interaction with the substrate and the surrounding fluid. This situation is depicted in Fig. 1. The attractive forces can be of different nature depending on the environment around the particle/surface system. For instance, van der Waals forces are always present while capillary forces only occur in atmospheric environment where the relative humidity is high enough to induce capillary bridges between surfaces in contact. Moreover, electrostatic forces can appear when the particle and/or the surface possess an electric charge. These electrostatic forces can thus be attractive or repulsive depending on the charges on each surface. Furthermore, the aerodynamic torque depends on the properties of the fluid (absolute pressure, density, viscosity) and the flow regime (laminar or turbulent). The combination of these forces makes the description of the resuspension phenomenon relatively complex and many physical models have been proposed over the years to describe the phenomenon. Theoretical models for particle resuspension have for the most part been developed by simply considering the case of isolated spherical particles deposited on a flat surface. Some approaches are based on the concept of turbulent energy transfer to the particle and a balance of potential energy (sometimes called vibrational) acquired by the particle to detach from the surface (Biasi et al., 2001; Reeks & Hall, 2001; Wen & Kasper, 1989; Zhang et al., 2013). These models are probabilistic and aim to simulate the probability density function (PDF) of certain variables of interest related to the particles. They present a kinetic approach to the phenomenon of resuspension in that they introduce the movement of particles around a pivot point on the surface. More recently, extended descriptions of the resuspension phenomenon have been proposed by Guingo and Minier (2008) and Henry et al. (2012) by considering the displacement of the particle on the wall after its rupture of equilibrium. These new models can be classified as dynamic models in the sense that they no longer consider the rupture of equilibrium as the resuspension event but integrate a refined description of the particle's trajectory on the surface and its interaction with the surface roughness to determine, in a probabilistic manner, the detachment of the particle. The reader interested in a history and a deepening of these subjects can refer to the work of Ziskind (2006) and Henry and Minier (2014) which offer exhaustive reviews on resuspension models. Another common approach is based on a force-balance concept where resuspension occurs after a disruption of the force (or moment) balance between the adhesion and the aerodynamic forces (moments). These types of models are commonly referred to as static force-balance approaches (Benito et al., 2015; Braaten et al., 1990; Ibrahim et al., 2003; Soltani & Ahmadi, 1994) in the sense that the detachment of the particle occurs as soon as the balance of forces is broken. These models admit that the particle lies entirely in the boundary layer of the air flow and is subjected to the following four forces: the aerodynamic drag (F_D) and lift (F_L), the force of gravity $F_g = m_p g$ and the adhesion forces F_{adh}. The description of the reentrainment of the particles is then carried out according to three modes of detachment which combine a balance of forces and moments around a pivot point. These three modes of detachment are detailed as follow:

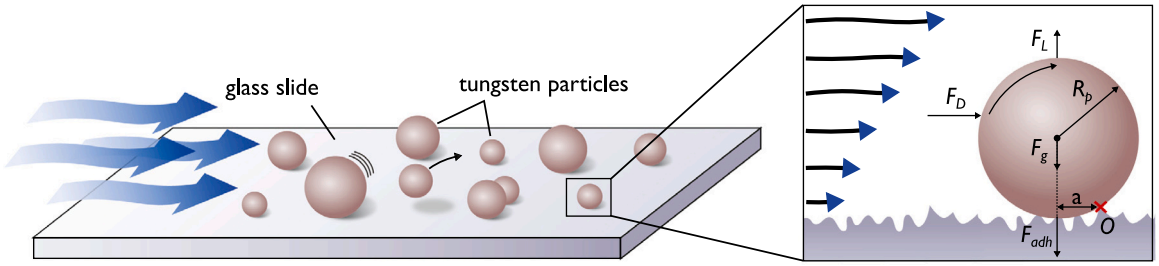

Fig. 1. Spherical tungsten particles deposited in a monolayer and exposed to a turbulent air flow.

- direct vertical lift-off which implies $F_L > F_{adh} + F_g$;
- sliding of the particle on the surface: $F_D > k_s(F_{adh} + F_g - F_L)$ with k_s the static friction coefficient;
- and rolling: $(1.4R_p)F_D + aF_L > a(F_{adh} + F_g)$ with R_p the radius of the particle and a the lever arm taken as the radius of the contact area between the particle and the surface.

Here, the adhesion force can be a combination of van der Waals (F_{vdW}), capillary (F_c) and electrostatic forces (F_e), i.e. $F_{adh} = F_{vdW} + F_c + F_e$. Although generally present in systems studied at atmospheric pressure, capillary forces will not be considered in the rest of the paper since the experiments were all performed keeping the relative humidity below 10% using dry air for the AM tests and an hermetic enclosure fed with nitrogen for the AFM measurements. In the first two modes, i.e. lifting and sliding, resuspension occurs when the aerodynamic forces overcome the adhesion forces in the normal and tangential direction, respectively. On the other hand, detachment by rolling occurs when the moment of aerodynamic forces ($\mathcal{M}_O(F_{\text{aero}}) = 1.4R_pF_D + aF_L$ where the factor 1.4 accounts for the anisotropy of the fluid near the surface) overcomes the moment of adhesion forces ($\mathcal{M}_O(F_{adh}) = aF_{adh}$) around a pivot point O located at a distance a from the particle-surface contact point (see Fig. 1). Among the three modes of detachment listed above, it has been shown that the mode known as "rolling" is mainly responsible for the detachment of particles embedded within the viscous sublayer (see e.g. Brambilla et al., 2017; Ibrahim et al., 2008; Soltani & Ahmadi, 1994; Villagrán Olivares et al., 2022), i.e. when $R_p^+ < 4$ with $R_p^+ = (R_p u_\star)/\nu$ the dimensionless radius of the particle. In addition, for the particle sizes considered in this study, the force of gravity F_g is several orders of magnitude lower than the van der Waals forces and can therefore be neglected. The rolling mechanism can thus be rewritten as:

$$\left(\frac{1.4R_p}{a}\right) F_D + F_L > F_{adh}. \tag{1}$$

Detachment of the particle thus only depends on the particle's size, the contact radius, its adhesion forces (which tend to prevent motion) and the aerodynamic drag and lift. The following paragraphs provide a short description of these forces.

1.1. Aerodynamic drag and lift forces

For a spherical particle deposited on a surface, the drag force is parallel to the surface. In the case where the flow is viscous, O'Neill (1968) determined that the drag force exerted on a sphere in contact with a flat surface can be expressed as $F_{D\parallel} = \frac{\pi}{2}\rho u_\star^2 R_p^2 C_{D\parallel}$, with $C_{D\parallel} = 24/Re_p$ the drag coefficient in the Stokes regime, $\rho = 1.293\ \text{kg m}^{-3}$ the density of the fluid and $u_\star$ the friction velocity defined by $u_\star = \sqrt{\tau/\rho}$ with τ the shear stress. The Reynolds number of the particle (Re_p) is defined by $Re_p = (R_p u_p)/\nu$ with $\nu = 1.51 \times 10^{-5}\ \text{m}^2\ \text{s}^{-1}$ the kinematic viscosity of the surrounding fluid and u_p the particle's velocity. In the present study, the value of the drag coefficient $C_{D\parallel}$ needs to be adjusted from the Stokes regime since the particle's Reynolds number can be higher than 1 (for particles with diameters between 10 µm and 20 µm and air flow friction velocities between $0.1\ \text{m s}^{-1}$ and $3\ \text{m s}^{-1}$, $0.1 \leq Re_p < 5$). For Reynolds numbers higher than unity, several semi-empirical correlations have been proposed and can be found in Fillingham et al. (2019), Henry and Minier (2014). For our particular case where $Re_p < 5$ the analytical formula derived by Liu et al. (2011) will be used and is given by:

$$C_{D\parallel} = f\frac{24}{Re_p}\left(1 + 0.0916Re_p\right), \tag{2}$$

with $f = 1.701$ a correction factor accounting for the presence of the wall. The drag force can thus be rewritten as:

$$F_{D\parallel} = 12\pi f \eta u_\star R_p \left(1 + 0.0916Re_p\right), \tag{3}$$

where $\eta = 1.8 \times 10^{-5}$ Pa s is the dynamic viscosity of the fluid in normal conditions. Similarly, the lift force in the normal direction is expressed as a function of the particle's Reynolds number and various analytical formulas were proposed depending on the size of the particles and their immersion in the viscous sub-layer. For the range of particle sizes and friction velocities used in our study, the empirical formula of Mollinger and Nieuwstadt (1996) can be used and is expressed by:

$$F_L = (56.9 \pm 1.1)\,\nu^2\rho\left(\frac{Re_p}{2}\right)^{1.87\pm0.04}. \tag{4}$$

1.2. Adhesion forces

1.2.1. The Hamaker approach

The study of the adhesion forces acting on solid particles whose sizes are between hundreds of nanometers and several micrometers involves several physical forces but is mainly governed by surface effects. Indeed, for such small objects, the force of gravity becomes negligible compared to the forces of adhesion. For example, the van der Waals forces are of quantum origin but have an important (and measurable) influence on microscopic objects when they are sufficiently close together (from few angstroms to few nanometers). This transition between the molecular (or atomic) world and the microscopic world is generally referred to as a bottom-up approach because the interaction force acting between each atom of a micrometer particle and a plane are described individually at the molecular scale (Alvo et al., 2010; Parsegian, 2005; Walton, 2008). The van der Waals forces are often calculated as the sum of the force between all pairs of interacting molecules and was first performed by Hamaker (1937). This macroscopic approach necessitate to integrate the overall interaction force on the total volume of the object which makes the calculation dependent on its shapes (Parsegian, 2005). For a spherical particle resting on a perfectly smooth surface the non-retarded van der Waals force is given by the following approximated formula:

$$F_{vdW} = \frac{AR_p}{6z_0^2}, \tag{5}$$

where A represents the Hamaker constant (J) which depends on the nature of the materials in contact and the environment in which they are found and z_0 the minimal distance between the objects. For smooth surfaces in contact, the minimum contact distance z_0 is generally taken between 0.2 nm and 0.4 nm (Israelachvili, 2011). The definition of the contact, and in particular the determination of the value of z_0, remain however an open issue.

1.2.2. Contact mechanic approaches

Other approaches, often referred to as top-down, are based on a macroscopic view of adhesion based on surface energies. The models best known using this approach are those of Johnson et al. (1971) (JKR) and Derjaguin et al. (1975) (DMT).

The JKR approximation. The JKR model is based on the assumption that the contact area between a spherical particle and a flat surface is enlarged by surface forces. This deformation is evaluated considering the Hertz theory for deformation and the action of surface forces only within the contact area. For a spherical particle in contact with a smooth surface, the JKR model gives the contact radius a_{JKR} between the two objects:

$$a_{\mathrm{JKR}}^3 = \frac{R_p}{K}\left(F + 3\pi\Delta\gamma R_p + \left[6\pi\Delta\gamma R_p + \left(3\pi\Delta\gamma R_p\right)^2\right]^{1/2}\right), \tag{6}$$

where $\Delta\gamma = \gamma_1 + \gamma_2 - \gamma_{12}$ is the Dupré equation giving the work of adhesion ($\mathrm{J\,m^{-2}}$) between the two materials in contact with surface energies γ_1 and γ_2 and interfacial energy γ_{12}. When the two materials are in contact without capillary bridge, the work of adhesion can be approximated by $\Delta\gamma = \gamma_1 + \gamma_2$ or $\Delta\gamma = 2\gamma$ if the two objects are identical in nature. In Eq. (6) the composite Young's modulus K is defined by:

$$K = \frac{4}{3}\left[\frac{1-\upsilon_1^2}{E_1} + \frac{1-\upsilon_2^2}{E_2}\right]^{-1}, \tag{7}$$

where E_i is the Young's modulus and υ_i is the Poisson's ratio of the material i. For zero mechanical stress ($F = 0$), corresponding to the moment when the detachment force is equivalent to the adhesion force, the radius of the point of contact a_{JKR} is given by:

$$a_{\mathrm{JKR}} = \left(\frac{6\pi\Delta\gamma R_p^2}{K}\right)^{1/3}. \tag{8}$$

In addition, the detachment "pull-off" force F_{po} (opposed to the adhesion forces) required to remove a particle from the surface is expressed by the JKR model as:

$$F_{\mathrm{JKR}} = -F_{\mathrm{po}} = -\frac{3}{2}\pi\Delta\gamma\ R_p. \tag{9}$$

The DMT approximation. Derjaguin et al. (1975) proposed an alternative model for adhesion called the DMT model. This model takes into account molecular attraction outside the contact zone but is limited to contact between a spherical particle and a solid flat surface. It establishes how the shape of the particle changes under the effect of contact deformations. The adhesion force then corresponds to the moment when the deformation generated by the contact forces is zero. In the case of a sphere on a plane surface, the contact radius a_{DMT} is written:

$$a_{\mathrm{DMT}} = \left(\frac{R_p}{K}\left(F + 2\pi\Delta\gamma\ R_p\right)\right)^{1/3}. \tag{10}$$

When the contact radius becomes zero, the pull-off force is then expressed simply by:

$$F_{\mathrm{DMT}} = -F_{\mathrm{po}} = -2\pi\Delta\gamma\ R_p. \tag{11}$$

Table 1
Properties of the materials used in this study.

	Poisson's ratio	Young's modulus (GPa)	Hamaker constant (10^{-20}J)	Surface energy (J m^{-2})
Tungsten	0.28	406	~37–50	~0.3–0.4
Glass	0.25	69	6.6	0.06

It can be seen that the adhesion force expressed by the DMT model gives a value 25% greater than the JKR model. Moreover, Eqs. (9) and (11) are independent of the elasticity criterion K but only function of the radius of the particle and the work of adhesion between the two objects. The debate on the validity of the JKR and DMT theories lasted until Tabor (1977) and Maugis (1992) showed that they were extreme cases of a dimensionless parameter μ_T given by:

$$\mu_T = \left[\frac{8\Delta\gamma^2 R_p}{9K^2D^3}\right]^{1/3}, \tag{12}$$

with D the distance between the particle and the surface. This dimensionless parameter μ_T can be interpreted as the relationship between the elastic deformation of the objects and the action of the adhesion forces. Thus, if $\mu_T \ll 1$ the model to use is DMT, corresponding to a small rigid particle. If on the contrary, $\mu_T \gg 1$, the model to use is JKR, corresponding to a coarse elastic deformable particle. The material's properties used in this study are given in Table 1. For the tungsten micro-spheres used in this work, the parameter μ_T is always greater than unity indicating that the JKR model should be used. Using these material's properties, a composite Young's modulus of 84 GPa is found for a tungsten/glass interaction. As we have just seen, the use of these contact mechanic models also requires to determine the work of adhesion $\Delta\gamma$ which depends on the surface energies of materials in contact. In the following paragraph we recall how it can be derived from the Hamaker constant of the materials using Hamaker theory.

1.3. The work of adhesion

This paragraph deals very briefly with the calculation of the surface energy of adhesion as presented by Israelachvili (2011) which we recommend to consult for more detailed explanations. Consider two solids S1 and S2, the summation of the energies of interaction between pairs of atoms for all the atoms of a solid S1 with all the atoms of a solid S2 separated by a distance D gives the following interaction energy $\omega = -A/12\pi D^2$. If the summation is done by including the interactions between pairs of atoms of the same solid, a second term must be added to the equation. This second term corresponds to the cohesion energy of the atoms constituting the solid with their immediate neighbors, that is to say for $D = z_0$. Thus, the total energy of adhesion to be considered for the two solids is:

$$\omega = -\frac{A}{12\pi}\left(\frac{1}{z_0^2} - \frac{1}{D^2}\right) = -\frac{A}{12\pi z_0^2}\left(1 - \frac{z_0^2}{D^2}\right) \text{ by surface unit.} \tag{13}$$

For $D = z_0$, this energy is zero (the surfaces are in contact) but for $D \to \infty$, Eq. (13) can be simplified by $\omega = -A/12\pi z_0^2 = 2\gamma$ thus giving the adhesion surface energy $\gamma = A/24\pi z_0^2$. Thereby, the surface energy of a solid is equal to half the energy required to separate two unit areas, or half the energy of adhesion. This result was obtained using the Hamaker method valid for a summation between pairs of atoms of two solids located at a relatively large distance D from each other. But in the case of contact, this method by summation raises again the choice of the contact distance z_0. Indeed, it has been shown by Tabor (1977) and Israelachvili (2011) that it is necessary to adapt Eq. (13) with a molecular approach accounting for the geometric arrangement of atoms present at the surface of solids. The "cut-off" distance z_0 thus becomes less than the inter-atomic distance β between the centers of two atoms in "contact". For example, for an inter-atomic distance $\beta = 0.32$ nm (corresponding to the lattice parameter of crystalline tungsten), Israelachvili (2011) recommends using a cut-off distance of $z_0 = \beta/2.5 = 0.128$ nm. The adhesion surface energy can therefore be rewritten as $\gamma = A/\left(24\pi\,(\beta/2.5)^2\right)$. For tungsten, Tolias (2018) calculated a theoretical Hamaker constant of 50×10^{-20} J which gives an adhesion surface energy of 0.4 J m^{-2}. Moreover, our previous AFM study in atmospheric conditions (Peillon et al., 2019) gave an effective Hamaker constant of 37×10^{-20} J for tungsten which gives a surface energy of 0.3 J m^{-2}. Recall that such values obtained within the framework of Hamaker's theory which only takes into account the van der Waals forces are much lower than the values which take into account metallic bonding between atoms. For example, an adhesion surface energy between 4 J m^{-2} and 4.6 J m^{-2} was calculated by Vitos et al. (1998) according to the crystal arrangement of a tungsten surface. Moreover, Tyson and Miller (1977) carried out surface tension measurements for liquid tungsten and reported an adhesion surface energy of 3.26 J m^{-2}. For the present work such high values of surface energy that considers metallic bonding are irrelevant and we will consider the values based only on the van der Waals interaction. Using the value of 6.6×10^{-20} J given by Das et al. (2007) for the Hamaker constant of SiO_2, we find a work of adhesion of $\Delta\gamma \approx 0.36$–$0.46$ J m^{-2} for a tungsten-glass interaction. One can also derive the theoretical Hamaker constant for this system with the following relation $A_{W/SiO_2} = \sqrt{A_W \times A_{SiO_2}} \approx 18 \times 10^{-20}$ J or an effective Hamaker constant $A^{eff}_{W/SiO_2} \approx 16 \times 10^{-20}$ J depending on the tungsten's Hamaker constant chosen for the calculation.

1.4. Taking surface roughness into account

The previous paragraphs showed that Hamaker's theory and the JKR/DMT models can be used to describe the adhesion of a spherical particle resting on a flat surface. However, these models do not take into account the roughness of the contacting surfaces which causes non-uniform deformation at the point of contact. But however small it may be, roughness is always present in real surfaces and must be accounted for when measuring adhesion forces (Henry & Minier, 2018; Prokopovich & Starov, 2011). Numerous studies have shown that the existence of nanometer (Jacobs et al., 2013; Kumar et al., 2013; Rabinovich et al., 2000a) and micrometer (Beach et al., 2002; Dejeu et al., 2010; Götzinger & Peukert, 2004) roughness induces a significant decrease in the adhesion between two objects due to a reduction in the area effectively in contact between the two surfaces and to an increase in the distance between the objects. In our previous AFM study (Peillon et al., 2019), a detailed description of the Rabinovich et al. (2000b) model as well as its validation against experimental data has been done. This analytical model is based on a Hamaker summation approach and considers hemispherical asperities on the surface which are defined by few parameters namely, the root-mean-square rms surface roughness and the peak-to-peak distance λ_s. The adhesion force is expressed as follows (Rabinovich et al., 2000b):

$$F_{adh} = \frac{AR_p}{6z_0^2}\left[\frac{1}{1+58\frac{rms R_p}{2\lambda_s^2}} + \frac{1}{\left(1+1.82\frac{rms}{z_0}\right)^2}\right], \tag{14}$$

where the first term in brackets represents the interaction between the particle and an asperity and the second term accounts for the interaction outside the contact area between the particle and the average surface plane. As noted by Rabinovich et al. (2000a) this approach is only valid for non-deformable objects and surfaces. For soft materials in contact, authors proposed to replaced the first term in bracket of Eq. (14) by the adhesion force between two spheres as determined by the JKR theory:

$$F_{adh}^{\mathrm{JKR}} = \frac{3\pi\Delta\gamma R_p r}{2\left(r+R_p\right)} + \frac{AR_p/6z_0^2}{\left(1+1.82\frac{rms}{z_0}\right)^2}, \tag{15}$$

with $r = \lambda_s^2/(58rms)$ the radius of the asperity as defined by Rabinovich et al. (2000a).

Since then, other approaches have been proposed to model the adhesion force between a spherical particle and a rough surface. In particular, You and Wan (2013, 2014) considered that the roughness of a surface can be described using fractal theory and a multiscale approach for the definition of the roughness distribution. Once the rms distribution is known, the adhesion force distribution between a particle and a rough surface can be obtained by integrating the distribution of the rms roughness into a mean adhesion force model. They then derived a JKR-based model to describe the van der Waals interaction:

$$F_{adh} = \frac{C^{3/2}Ka_{\mathrm{JKR}}^3}{3R_p} \qquad C = \frac{1}{2}\left[\mathrm{erf}\left(\frac{\delta_1+\delta_2-2.7\times rms}{\sqrt{2\left(rms^2+rms_p^2\right)}}\right)+1\right] \tag{16}$$

where C is a factor accounting for the effect of surface roughness toward the contact area and rms_p is the roughness of the particle. In Eq. (16), $\delta_1 = a_{\mathrm{JKR}}^2/3R_p$ and $\delta_2 \approx 0.825\times\delta_1$ are the approach and extension distances between the center of the particle and the point of contact due to adhesion forces. Following the same methodology, Sun et al. (2021) recently developed a simplified JKR-based model which only considers the mean rms roughness of the substrate having asperity heights described by a Gaussian distribution. The derived expression for adhesion force is the same as in Eq. (16) but the factor accounting for surface roughness is simplified:

$$C_A = \frac{1}{2}\left[1-\mathrm{erf}\,\frac{k_A\times rms-\delta_N}{\sqrt{2rms^2}}\right], \tag{17}$$

where $\delta_N = a_{\mathrm{JKR}}^2/R$ is the overlap deformation between the asperity and the particle due to adhesion forces, with $R = \left(1/r+1/R_p\right)^{-1}$ the reduced radius. The model parameter $k_A \approx 1.82$ is a scaling factor accounting for the uncertainty of the asperity heights dispersion. These different models will be compared to experimental adhesion force measurements later on in Section 4.

1.5. Electrostatic image force

To complete the description of the forces involved in the adhesion of particles in the present study, it is necessary to address here the role of electrostatic forces. In fact, most of the time, micro-particles of natural or artificial origin are electrically charged, the charging mechanisms being very diverse (friction, self-charging, spraying, ion diffusion, contact charge, thermionic or photoelectric emission, etc.). As recalled in the introduction, when a particle carries a radio-element such as tritium, the beta decay occurring inside the particle will electrically charge the particle through a process known as self-charging (Yeh et al., 1976). The importance of this phenomenon will depend on the radio-element, the specific activity, the size and the nature of the particle as well as the environmental conditions (Clement et al., 1994; Kim et al., 2016). The influence of the image force (due to self-charging) on the adhesion of radioactive materials has for example been shown by Walker et al. (2010) and Kweon et al. (2013) while levitation of tritiated graphite particles where qualitatively observed by Skinner et al. (2004) and Winter (2004). The specific activity carried

by the particle is obviously a determining factor in the appearance of the electrostatic image force that we will further comment at the end of Section 4. For the specific case of a charged dielectric particle in contact with a dielectric substrate, an image charge will appear in the substrate thus creating an electric field that will induce the polarization of the particle which itself causes the appearance of a new image charge in the substrate and so on (Jones, 1995). If we consider that the charge distribution on the particle is homogeneous and that there is no external electric field, a dielectric charged particle deposited on a dielectric substrate will experience an electrostatic image force towards the substrate expressed by Hays and Sheflin (2005) as:

$$F_{im} = \alpha\left(\kappa_p, \kappa_s, \kappa_m\right) \frac{QQ'}{16\pi\epsilon_m\left(R_p + z_0\right)^2} \qquad \text{with} \qquad Q' = Q\frac{\kappa_s - \kappa_m}{\kappa_s + \kappa_m}, \tag{18}$$

where Q is the charge carried by the particle, Q' is the magnitude of the image charge induced in the substrate, κ_s, κ_p and κ_m are the relative permittivity of the surface, the particle and the medium respectively and α is a correction factor accounting for the particle polarization. In Eq. (18), the permittivity of the medium ϵ_m is defined by $\epsilon_m = \kappa_m\epsilon_0$ with $\epsilon_0 = 8.85 \times 10^{-12}$ F m^{-1} the permittivity of vacuum.

2. Atomic force microscopy measurements

Unlike indirect measurement techniques (aerodynamic, centrifuge, electrostatic), force measurements made with an AFM only concern a single particle of fixed size. To be as representative as possible of the interaction between a large number of particles of the same size with the chosen substrate, it is therefore necessary to have a very large number of force measurements on relatively large areas with a single particle. This provides a statistical description of the behavior of a population of particles of the same size but deposited at different locations on the surface. In the case of spherical particles, the adhesion force distributions thus obtained can then be adjusted using continuous statistical laws which are directly related to the statistical distribution of the roughness of the surface (Götzinger & Peukert, 2004; You & Wan, 2014; Zhou et al., 2003). The following paragraphs present the experimental method used to determine the statistical law describing the roughness of the glass substrate and how to measure the adhesion force distributions of the tungsten micro-spheres by AFM.

2.1. Preparation of samples and experiments

Adhesion force measurements have been realized with a Multimode 8 (Bruker™) AFM in PeakForce Quantitative Nano-Mechanical mode (PF-QNM) at ambient pressure. To avoid moisture and the formation of unwanted capillary bridges between the particle and the glass substrate, the AFM was positioned inside an hermetic glass enclosure fed with nitrogen. The relative humidity was monitored in real time with a Sensirion SHTC3 sensor. During the measurements, relative humidity levels of 3–9% were achieved. The measurements were realized between tungsten micro-spheres with three different sizes glued onto tip-less CP-FM (Colloidal Probe for Force Modulation) cantilevers and a glass substrate. The glass sample was cleaned by successive ultrasonic baths of acetone and ethanol and dried before being mounted in the AFM. Tungsten particles were purchased from Tekna Advanced Materials™ which produces metallic powders by a RF plasma discharge technique (Jiang & Boulos, 2006). This same powder has been used in previous studies (Peillon et al., 2019, 2020) and is well characterized in terms of particle size distribution, chemical composition, density and specific surface area. The particle size distributions in number and volume measured with an AEROSIZER 3230 TSI™are reproduced in Fig. 2(a). The tungsten powder comes with a broad size distribution with spherical particles with diameters between 5 µm and 50 µm. A SEM micrograph of the stock tungsten powder is reproduced in Fig. 2(b). In order to perform the grafting of spherical particles with best control, a wet sieving method has been used in order to reduce the broadness of the particle size distribution. After this step, batches of powders with narrower particle size distributions were used for functionalization of the cantilevers and for the aerodynamic method tests presented later on in the paper. Tungsten spherical particles of desired sizes were then grafted on AFM tip-less cantilevers using optical microscope, micro-manipulator and epoxy glue following method introduced by Ducker et al. (1991) and well detailed by Gan (2007). The grafted particles were checked with a JEOL JSM-6010 Scanning Electron Microscope (SEM) before and after the experiments in order to measure the diameters of the particles and to verify the absence of contamination on the particles. Figs. 2(c)–2(e) show SEM micrographs of these particles once attached to the AFM cantilevers. Three diameters were studied: 7 µm, 15 µm and 20.7 µm. SEM analysis also highlighted that surface roughness of the particles is negligible and that no plastic deformation was visible after the experiments. The error on the diameter measurement with SEM is relatively small and is equal to 0.1 µm for all the particles measured. The next step was to characterize the roughness of the glass surface on which the adhesion measurements were carried out.

2.2. Characterization of the glass roughness

The glass slide roughness was measured with the AFM in ScanAsyst mode (Bruker) using standard Silicon-Nitride AFM tip. The scan has a size of 20 × 20 µm^2 with a resolution of 820 × 820 pixels (i.e. 24 nm/pixel), and is depicted in Fig. 3(a). A common practice to describe the roughness is to calculate its root mean square (*rms*) value. Although it is possible to use the mean *rms* roughness of the total scanned area, in this case 400 µm^2, it is also possible to divide the surface into subareas that have the same dimensions of the contact radius of the particles studied. Such an approach means that there will be a distribution of *rms* roughness over the surface and that a single particle will experience a different *rms* roughness depending on its location (You & Wan, 2014). For the tungsten micro-spheres studied, the JKR theory gives contact radii between 107 nm and 221 nm, i.e. disk surfaces between

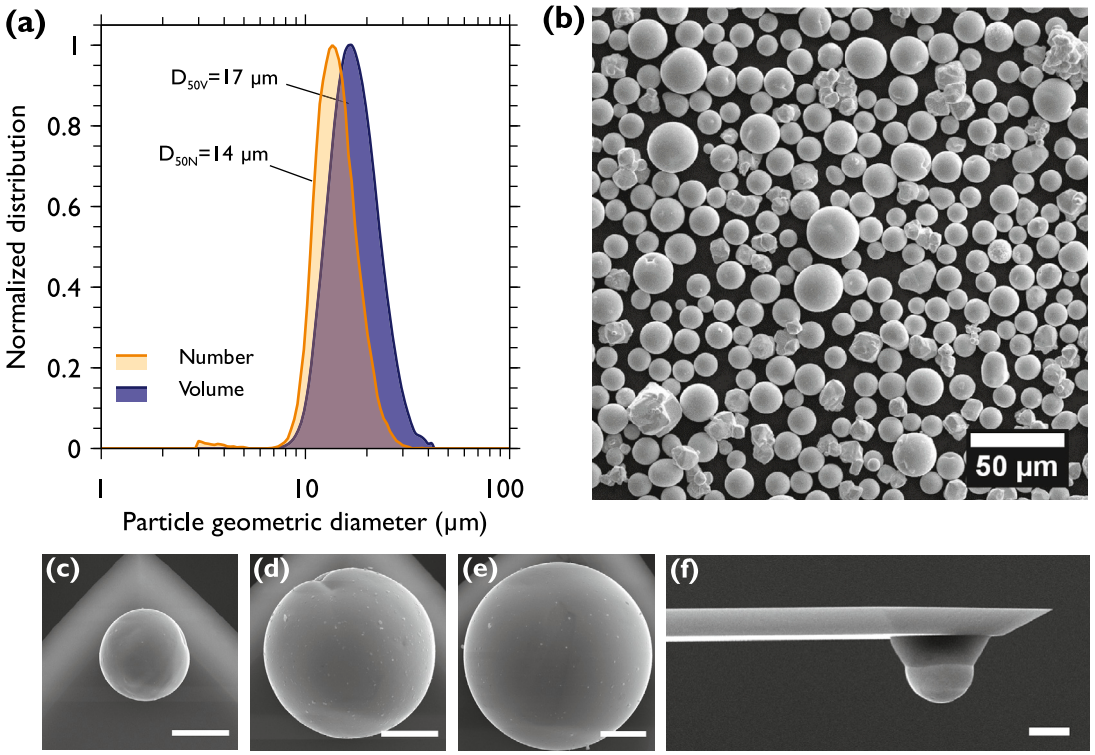

Fig. 2. **(a)** Particle size distributions in number and in volume of the tungsten powder. **(b)** SEM micrograph of tungsten powder. Spherical tungsten particles grafted onto tip-less cantilevers with diameters of 7 μm **(c)**, 15 μm **(d)** and 20.7 μm **(e)**, respectively. **(f)** Side view of a particle glued onto the cantilever. Scale bars are all 5 μm in length.

$0.04\,\mu m^2$ and $0.15\,\mu m^2$, which correspond approximately to $10-16$ squared pixel areas in the AFM scan image. In order to divide the scan into a finite number of subareas, squared subareas of 20×20 pixels were chosen for the analysis. This yields a total of 41×41 subareas of $0.23\,\mu m^2$ each. A MATLAB subroutine was used to split the scan image and calculate the *rms* roughness in each of the 1681 subareas thus created. The *rms* roughness distribution of these subareas is represented in Fig. 3(b). Although the height distribution of a surface generally follows the normal law (Götzinger & Peukert, 2004), it is not the same for the distribution of the *rms* roughness and some studies have suggested that it is better approximated by either log-normal, Weibull or gamma continuous distributions (Sun et al., 2021; You & Wan, 2013). In the present case the best fit was obtained with the log-normal (LN) distribution also depicted in Fig. 3(b). In the following, we thus propose to use the analysis procedure developed by You and Wan (2014) to do a statistical description of the *rms* roughness of the substrate and the adhesion force distributions. If $x > 0$ is a random variable representing the *rms* roughness, the cumulative distribution function (CDF) of its LN distribution is expressed by:

$$f_{rms}(x,\mu,\sigma) = \frac{1}{2} + \frac{1}{2}\,\mathrm{erf}\left[\frac{\ln(x)-\mu}{\sigma\sqrt{2}}\right], \tag{19}$$

where μ and σ are the mean and standard deviation of the distribution if x is log-normally distributed. In this case, the arithmetic mean and standard deviation are expressed by $E[x] = \exp\left(\mu + \frac{\sigma^2}{2}\right)$ and $\mathrm{SD}[x] = \exp\left(\mu + \frac{\sigma^2}{2}\right)\sqrt{\exp(\sigma^2) - 1}$, respectively. One can also calculate the median of the distribution with $m[x] = \exp(\mu)$. For the present distribution, the following parameters are found: $\mu = 0.75$ and $\sigma = 0.26$ which give a mean *rms* roughness of 2.2 nm and a standard deviation of 0.58 nm. To complete the analysis of the surface texture, its typical wavelength (λ_s) was extracted using GWYDDION software from a height profile visible in Fig. 3(c). This profile has a width of 1 pixel and spans the entire image with a length of 20 μm. The average peak-to-peak distance of this profile is found to be $\lambda_s \approx 320$ nm.

2.3. Pull-off force measurements

The pull-off force measurements were realized with the PF-QNM mode which allows simultaneous imaging of topography and mechanical properties (elasticity, adhesion, deformation and dissipation) of the analyzed sample. Since the force applied to the sample by the tip is controlled, this mode also allows the production of force curves from which quantitative data on the properties of the material studied are extracted. In this mode, the cantilever oscillates at a frequency of 2 kHz allowing to make an image quickly while remaining well below the mechanical resonant frequency of the cantilever (generally around 70–80 kHz). The particle

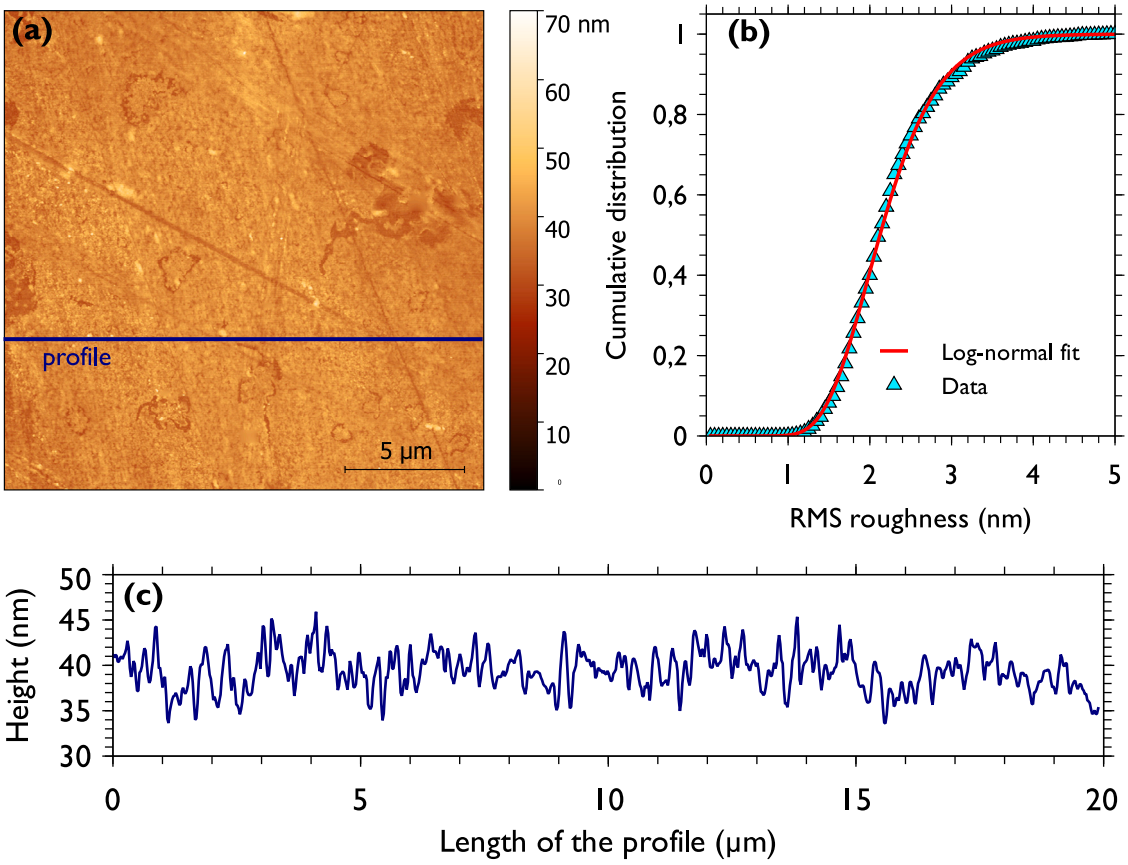

Fig. 3. **(a)** Topography image (20×20 µm^2) of the glass slide obtained by ScanAsyst mode with the AFM. **(b)** *rms* roughness distribution of subareas and its log-normal fit. **(c)** Height of a 1 pixel width profile across the topography image.

which is glued at the end of the cantilever touches the surface intermittently with a constant force on which the feedback loop of the microscope is set. The course of a PF-QNM measurement is conventionally explained by the force–distance curve depicted in Fig. 4(a). A diagram of the AFM principle is proposed in Fig. 4(b). The pull-off force is calculated using Hooke's law: $F_{\mathrm{po}} = \kappa \times \delta$ with κ being the spring constant of the cantilever (expressed in N m^{-1}) and δ (m) its vertical deflection extracted from the photodiode signal (in V) which is proportional to the displacement of the piezoelectric stage. The spring constant κ of a functionalized cantilever is measured using the Thermal Tune method provided by the AFM software. The Thermal Tune method calibrates the spring constant of a cantilever by fitting the power spectral density of the cantilever fluctuations with a known Lorentzian curve (Butt et al., 2005). The deflection sensitivity δ depends on the quality of the optical trajectory of the laser, reflectivity of the cantilever and environmental conditions.

2.4. Adhesion force distributions

For each particle size, an adhesion image with a minimum size of 10×10 µm^2 and a resolution of 128×128 pixels was produced. Therefore, for each adhesion image, 16,384 force values were obtained, giving in a single image a good statistical representation of the distribution of adhesion forces between the particle and the substrate. Example of adhesion images are given in Figs. 5(a)–5(c) for single tungsten particles with 7 µm, 15 µm and 20.7 µm diameter, respectively. For each particle size, three different areas of the glass substrate were scanned, thus yielding three adhesion force distributions for the same particle size. These three adhesion force distributions are visible in Figs. 5(d)–5(f). Although the particles are spherical and the glass surface has a low roughness, it can be seen that the adhesion force distributions of these micro-spheres have a relatively large dispersion. In addition, a variation in the mean and the standard deviation of the distributions obtained on the three areas can be observed. Each of these experimental adhesion force distributions was then fitted with a LN distribution. The location and scale parameters μ and σ of these log-normal fits are gathered in Table S1 of the supplementary materials together with the arithmetic mean $E_{i,j}$, median $m_{i,j}$ and standard deviation $\mathrm{SD}_{i,j}$ for a particle size i and a scan area j (numbered #1, #2 and #3 in Fig. 5 and in Table S1). For each particle size i, a mean LN distribution $f_{\mathrm{LN}}\left(\overline{\mu},\overline{\sigma}\right)$ was obtained by averaging the means $\left(\overline{\mu_i} = \frac{1}{3}\sum_{j=1}^{3}\mu_{i,j}\right)$ and variances $\left(\overline{\sigma_i} = \left[\frac{1}{3}\sum_{j=1}^{3}\sigma_{i,j}^2\right]^{1/2}\right)$ of

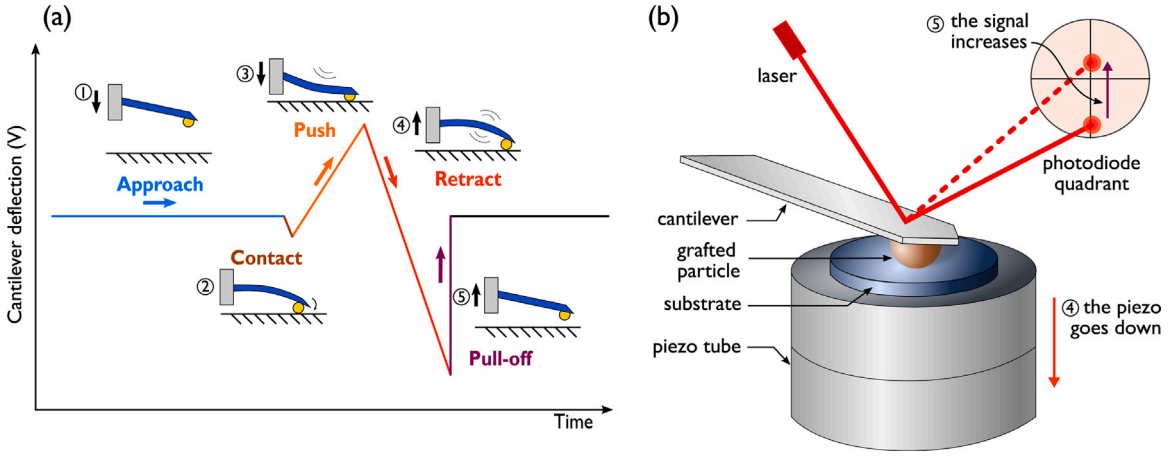

Fig. 4. **(a)** Principle of the PF-QNM measurement: (1) the tip approaches the substrate and instability due to van der Waals forces appears a few nanometers from the substrate. (2) The cantilever bends and the tip contacts the substrate. (3) The tip is then pushed against the substrate continuously until a previously set positive force (this is the PeakForce set point) is reached. (4) The tip is then retracted from the substrate at the same speed. During this withdrawal phase, the movement of the cantilever reproduces the curve initiated during the movement during phase (3). Due to the adhesion forces in the contact region, the tip does not separate from the substrate at the same point where the contact was made. (5) This results in additional negative force to detach the tip from the substrate and abrupt separation occurs. This pull-off force corresponds to the total adhesion force one seeks to measure. **(b)** Diagram of the AFM force measurement principle with a particle grafted beneath a tip-less cantilever. The deflection sensitivity δ depends on the quality of the optical trajectory of the laser, reflectivity of the cantilever and environmental conditions.

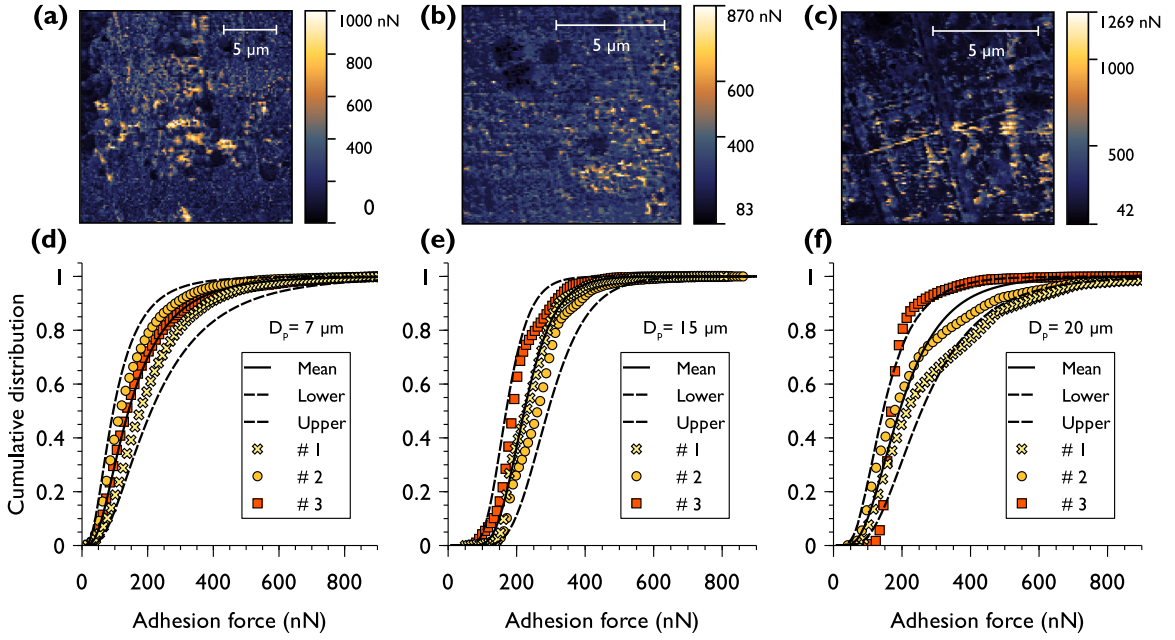

Fig. 5. Adhesion force images obtained in PF-QNM mode for **(a)** 7 µm, **(b)** 15 µm and **(c)** 20.7 µm diameter particles, respectively. Cumulative distributions of adhesion forces for three different measurements for each particle diameter: **(d)** 7 µm, **(e)** 15 µm and **(f)** 20.7 µm.

the three individual LN distributions obtained on three different scanned areas of the substrate. In order to reflect the variation of the measured adhesion force distributions from the three different scanned areas, an upper and lower LN distributions are added to the analysis in Figs. 5(d)–5(f). The upper and lower distributions are defined by adding or subtracting twice the standard deviation of the means for a particle size i, namely $\overline{\mu_\pm} = \overline{\mu_i} \pm 2S_i$ with $S_i = \sqrt{\frac{1}{3}\sum_{j=1}^{3}\left(\mu_{i,j} - \overline{\mu_i}\right)^2}$. Following this analysis, one can extract the means and standard deviations of the adhesion forces for the 7 µm, 15 µm and 20.7 µm diameter particles which are 178.5 ± 143.5 nN, 234.7 ± 74.6 nN and 230 ± 141.8 nN, respectively. These experimental mean adhesion forces can be compared to the values obtained with the Hamaker formula of Eq. (5) giving 1166 nN, 2500 nN and 3450 nN, respectively. It is therefore observed that a mean *rms* roughness as low as 2.2 nm leads to a reduction of more than an order of magnitude in the adhesion forces.

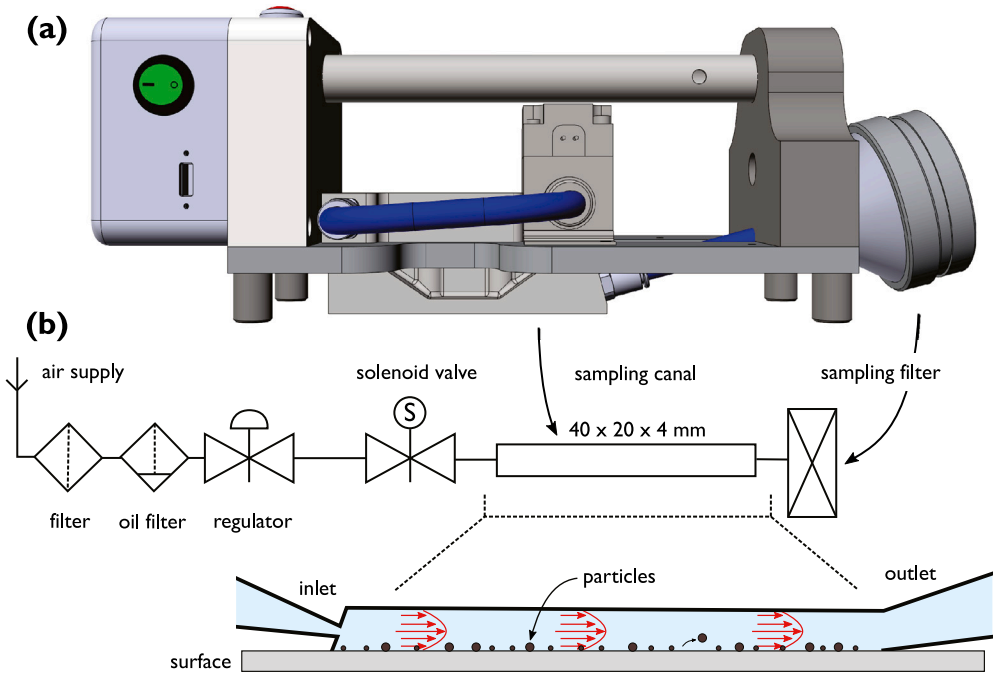

Fig. 6. **(a)** Schematic view of the side of the aerodynamic device and **(b)** the aeraulic diagram.

In order to compare the adhesion forces measured by AFM with those measured by the AM, it is rather convenient to derive the median of the adhesion force distributions obtained since the AM relies on the determination of the threshold friction velocity, i.e. the velocity for which 50% of the particles are resuspended, to deduce the median adhesion force of a population of particles. The aerodynamic method and the comparison between the two measurement techniques are presented in the following Sections 3 and 4.

3. Aerodynamic method

The results obtained in the previous section using an AFM can be compared to other methods allowing the estimating of adhesion forces of a deposit of particles. These so-called indirect methods are based on the measurement of a threshold force which is associated with the detachment of 50% of particles of the same size. In the present paper, the aerodynamic method was chosen since an aerodynamic device was already designed and built for sampling purpose (Peillon et al., 2020). The characterization of the air flows produced by the device is crucial for the calculation of the aerodynamic forces leading to the detachment of the particles and thus the evaluation of their adhesion via a balance of forces (moments). The design of the device and the numerical calculations of the friction velocities inside the device are presented hereafter.

3.1. Design of the aerodynamic device

The aerodynamic device (AD) is a very small rectangular channel in which a calibrated air flow is drawn. The current version of the device (see Fig. 6(a)) produces friction velocities ranging between $0.1\,\mathrm{m\,s^{-1}}$ to $3\,\mathrm{m\,s^{-1}}$ inside the sampling channel. The principle is to inject clean dry compressed air (between 0.5 and 2 bars) into the channel through a slit of a few millimeters. The channel has a sampling area of 20×40 mm^2 and a height of 4 mm. The compressed air is injected through a slit of 1×15 mm^2 forming an angle of 15° with the surface as depicted in Fig. 6(b). Indeed, in the case where the air flow is turbulent (the Reynolds number in the device is always greater than 4000 for the operating pressures chosen), Masuda et al. (1994) have shown that the more the impacting angle of the air jet is small relative to the surface, the larger the influence region of the jet, which permit to increase the particle detachment efficiency. The inlet pressurized clean air is controlled with the help of a solenoid valve and a pressure regulator. The flow can be continuous or pulsed with controlled opening time thanks to an ARDUINO™card that drives the solenoid valve. Detached particles are collected on a filter membrane installed downstream of the channel. This filter membrane can be used to sample particles but also makes it possible to avoid dispersing particles once they are resuspended. This feature is particularly useful when the particles studied are radioactive and contamination must be avoided. Since the geometry of the device is quite small and the air flows are important, free-stream velocities reach hundreds of $\mathrm{m\,s^{-1}}$ inside the channel. To better understand the different velocity areas that are forming inside the sampling channel, we performed numerical flow simulations using *Ansys CFX* software for a continuous flow with an air flow rate of $70\,\mathrm{L\,min^{-1}}$.

Table 2
Calculation parameters used for CFD simulations.

Parameter	Value
Turbulence model	k-ω SST model (Shear Stress Transport)
Numerical scheme	Hybrid scheme (High Resolution)
Convergence	Steady state calculation Number of iteration = 2000 MAX residuals = 10^{-6}
Timescale	Timescale control = local timescale factor Timescale factor = 3

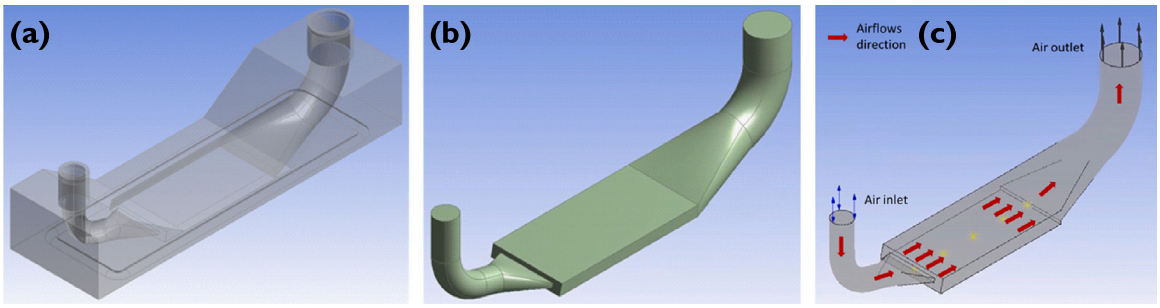

Fig. 7. **(a)** Geometry of the AD designed with Ansys Design Modeler software, **(b)** simplified design for CFD calculations and **(c)** boundary conditions location in AD.

3.2. Numerical simulations

This part will present the numerical (CFD) simulations of air flows in the AD. These calculations aimed at evaluating friction velocities at the surface for different inlet pressure conditions in order to quantify aerodynamic torque exerted on the particles along the aeraulic channel of the device.

3.2.1. Geometry and calculation domain

Calculations were carried out with ANSYS CFX software, a generalist commercial CFD code dedicated to resolve well-known Navier–Stokes fluid mechanics equations. The introduction of the Boussinesq hypothesis in the definition of eddy viscosity allows to model the shear stress tensor using turbulence models. The setup of CFD calculations consists of the following three steps: (i) geometry design and calculation domain definition, (ii) dataset definition (boundary conditions, numerical parameters and initial conditions) and (iii) calculations and post processing. Fig. 7(a) shows the design of the AD channel used for 3D printing and Fig. 7(b) the design implemented in ANSYS CFX to perform CFD calculations of air flows inside the device for *in-situ* conditions. This last design is simpler because for CFD calculations, only the fluid domain is needed, so the wall thickness were removed. Calculation progress consists in extracting air from the outlet of the AD in order to generate strong air flows allowing detachment of particles. Two openings are available on the AD, the first is the air inlet and the second is the air outlet as represented in Fig. 7(c). The air inlet is treated as an opening with an imposed relative pressure $P_r = 0$ Pa. At the air outlet a mass flow rate of $Q_{out} = 70\ \mathrm{L\,min^{-1}}$ is imposed while an automatic wall law is applied to the walls with no slip condition. Numerical parameters implemented for calculations are summarized in Table 2. The calculations were stationary in order to get a steady state of the air flows inside the AD. Two thousand iterations allowed to reach a very low level of RMS (Root Mean Square) and MAX residuals. For the timescale control, a local timescale factor of three was implemented, knowing that this control enables to adapt the timescale to velocity gradients in the fluid domain. After a sensitivity study, a SST k-ω turbulence model was chosen for these simulations compared to a k-ϵ model. Given the strong air flows and velocity gradients inside the AD, a hybrid numerical scheme was considered allowing to adapt automatically the numerical scheme order to spatial and time evolution of the velocity.

3.2.2. Derivation of friction velocities

The 20×40 mm^2 channel of the AD was divided into 10 segments of 12×4 mm^2 as shown in Fig. 8(a). The air inlet is at the position $x = 0$ on these diagrams. It can be seen that the air inlet zone ($x = 0$ mm to $x = 4$ mm) is very unstable with an average friction velocity of $2\,\mathrm{m\,s^{-1}}$ and a standard deviation of $1.5\,\mathrm{m\,s^{-1}}$. An area of 3 segments (from $x = 4$ mm to $x = 16$ mm) is then observed with high friction velocities around $2.5\,\mathrm{m\,s^{-1}}$; a zone where the friction velocity decreases from $2\,\mathrm{m\,s^{-1}}$ to $0.8\,\mathrm{m\,s^{-1}}$ (from $x = 16$ mm to $x = 28$ mm) and finally a zone of 3 segments where the friction velocity remains around $0.5\,\mathrm{m\,s^{-1}}$. The numerical data are represented by an histogram in Fig. 8(b) showing the means and standard deviations of friction velocities obtained in the 10 segments of 12×4 mm^2. Thanks to these numerical simulations we find that the small dimensions of the AD channel allow access to a relatively wide range of friction velocities. Indeed, these friction velocities correspond to high free-stream velocities between $25\,\mathrm{m\,s^{-1}}$ and $200\,\mathrm{m\,s^{-1}}$ and such an air flow range is rarely achieved in resuspension studies that use larger wind tunnels.

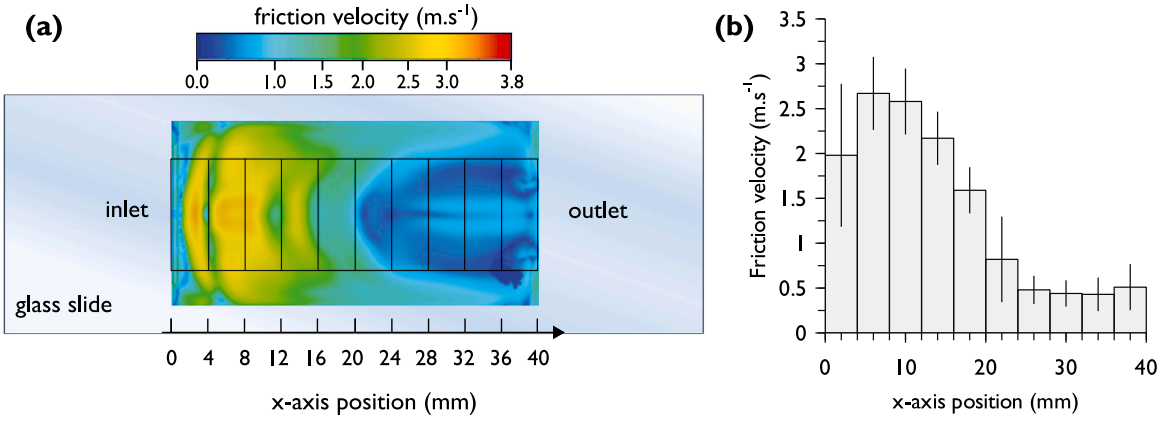

Fig. 8. **(a)** 2D mapping of the friction velocities produced by the AD for an airflow rate of 70 L min^{-1} for 10 segments of 4 mm width. **(b)** Averages and standard deviations of friction velocities obtained with CFX according to the x-axis position.

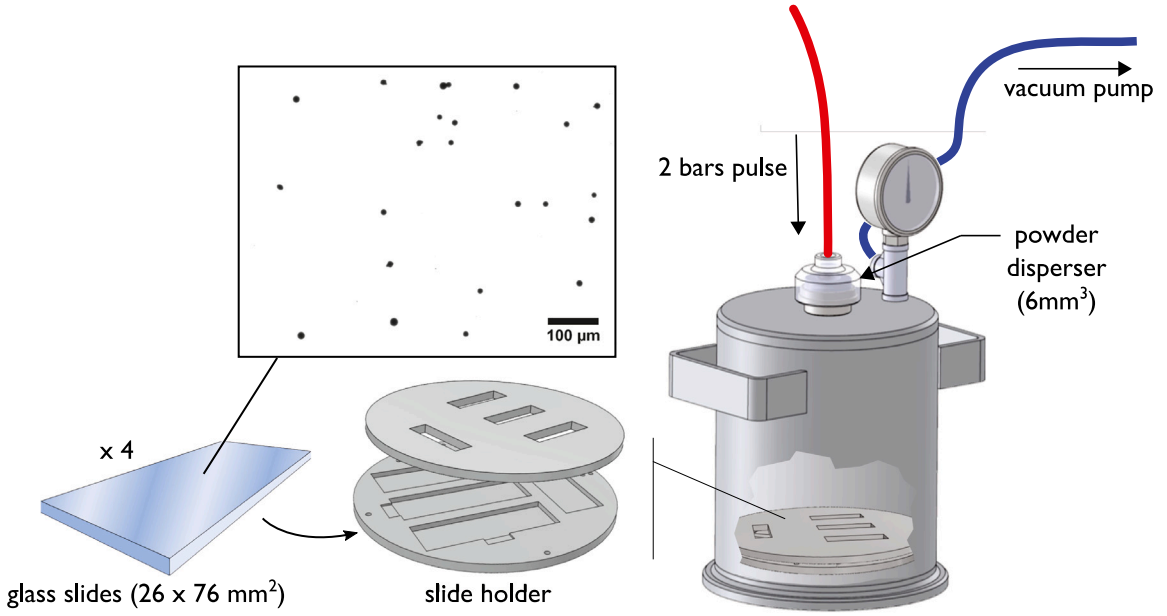

Fig. 9. Representation of the slide holder and the mask allowing the deposition of the particles on defined zones on four glass slides at the same time. The insert is a thresholded optical microscope image showing that individual particles are well separated on the glass slide.

3.3. Experimental procedure

The experimental procedure used to carried out resuspension experiments is detailed in the following. First, the tungsten powder is dispersed on standard microscope glass slides (26 × 76 mm^2) over an area of 20 × 40 mm^2 (800 mm^2) corresponding to the center area of the glass slide swept by the flow of the AD visible in Fig. 8(a). At each dispersion, four deposits are made at the same time using a custom glass slide holder accommodating the four microscope slides covered by a stainless steel mask visible in Fig. 9. To disperse the powder and make the deposits, the microscope slide holder is placed inside a dispersion bell 16 cm in diameter and 18 cm in height. A calibrated volume of powder (usually 6 mm^3) is placed through an orifice located at the top of the bell and is dispersed uniformly over 201 cm^2. The total area represented by the four deposits on the four glass slides is equivalent to 32 cm^2. It should be mentioned here that for these powder dispersion parameters, the surface concentration of the particles on the glass slide is between 1 mm^{-2} and 20 mm^{-2}. Such low surface concentration of particles mitigates potential collision effects leading to an increase in the resuspension of smaller particles as identified by Rondeau et al. (2021) and Banari et al. (2021) for higher surface concentrations. Once the deposits are made, the four slides are installed in a MORPHOLOGI G3 MALVERN™optical microscope slide holder to perform an initial count of the particles. A circularity filter (>0.97) is defined to count only the spherical particles. Likewise, particles with a diameter greater than 18 µm and smaller than 10 µm are removed from the count. Once this initial counting

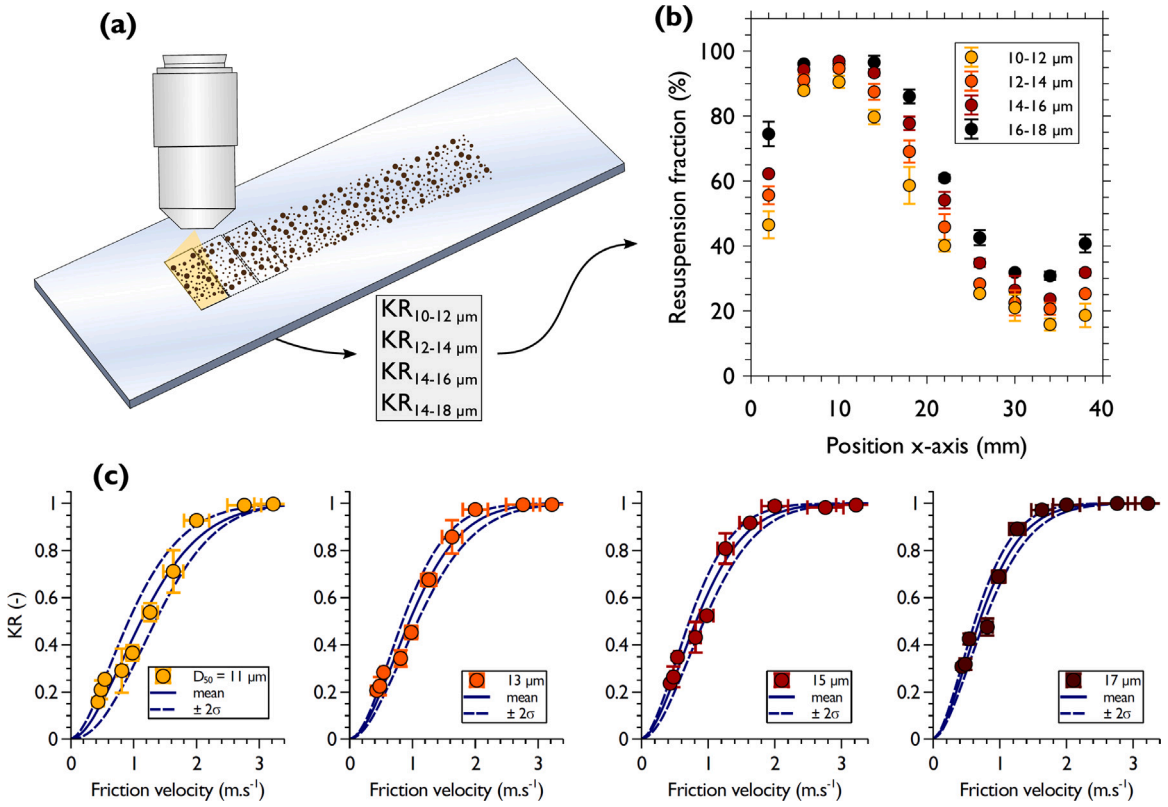

Fig. 10. **(a)** Diagram of the counting procedure with the optical microscope on the ten segments along the deposit. **(b)** Resuspension fractions obtained with the AD as a function of the position along the x-axis of the channel and for different particle size bins for an airflow rate of $70\,\mathrm{L\,min^{-1}}$. **(c)** Resuspension fractions versus friction velocity for the non-radioactive tungsten particles.

has been done, the four slides are successively placed in a custom-made support which makes it possible to expose a slide with dust deposit to the AD. The operating airflow rate of the AD ($70\,\mathrm{L\,min^{-1}}$) must be set before the test. The exposure time of the deposit of particles to the air flow is set to 10 s. The four deposits are exposed in the same way for the chosen flow configuration. They are then re-positioned in the microscope slide holder and the remaining particles on the glass slides are recounted with the same filters (sizes and circularity) as before.

3.4. Resuspension fractions

We present in Fig. 10(b) the resuspension fractions obtained for the non-radioactive tungsten particles regarding the position along the x-axis in the channel for four particle size bins ranging from $10\,\mu\mathrm{m}$ to $18\,\mu\mathrm{m}$ with a bin width of $2\,\mu\mathrm{m}$. This choice was motivated by the fact that a significant number of particles must be counted in each size bin in order to have a good statistical representation when performing repetition of the experiments. Results are expressed in terms of resuspension fraction KR_i, giving the ratio between the number of resuspended particles of size bin i: $\Delta N_i = N_{0,i} - N_{f,i}$ over the total number of particles of size bin i initially present in the deposit $N_{0,i}$ such as:

$$\mathrm{KR}_i = \frac{\Delta N_i}{N_{0,i}} = \frac{N_{0,i} - N_{f,i}}{N_{0,i}}, \tag{20}$$

with $N_{f,i}$ the number of particles of size bin i remaining on the glass slide after the experiment. In Fig. 10(b) each point represents the mean $\overline{\mathrm{KR}_i}$ and twice the standard deviation σ_i of the resuspension fractions obtained for four repetitions of the experiment for a specific particle size bin and a given position. By performing these numerous counts on the ten segments of the AD channel, it is found that particle detachment efficiency varies significantly depending on the region analyzed. For the same size bin, this efficiency can vary from 20% to 100% with a good repeatability. It can also be noted that the removal efficiency is systematically higher, at any point of the channel, for larger particles. In fact, progressing along the x-axis of the channel, it has been seen in Fig. 8(b) that the friction velocity decreases resulting in a decrease of the resuspension fractions which is well represented by the measurements given in Fig. 10(b) for the four particle size bins. However, it can be noted that the resuspension fractions obtained for segments 7, 8 and 9 (corresponding to the positions in the channel from $x = 24$ mm to $x = 36$ mm) decrease while the friction velocities in these

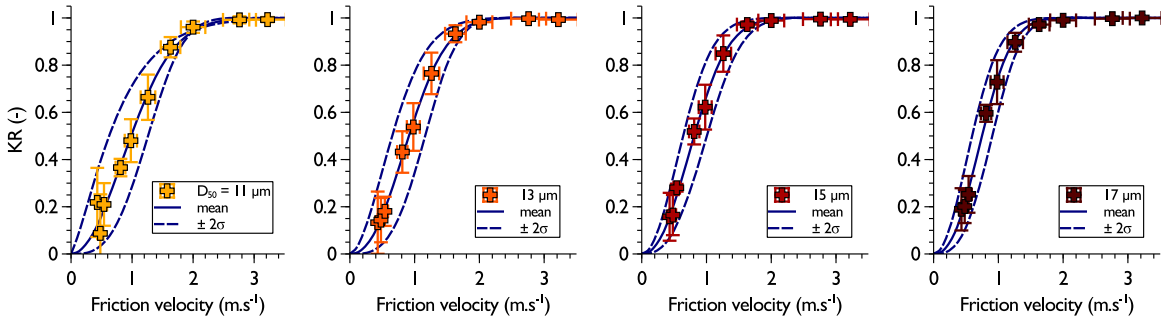

Fig. 11. Resuspension fractions versus friction velocity for the tritiated tungsten particles.

three segments are identical according to the CFD calculations of Fig. 8(b). One hypothesis that could explain such a result is that the particles having been detached at the beginning of the channel (i.e. between $x = 0$ mm and $x = 22$ mm) are redeposited downstream of the glass slides thus adding to the final count and reducing the actual resuspension fraction. Nonetheless, concerning the objectives of the work presented in this study, this re-deposition phenomenon has little importance except to increase the uncertainty on the resuspension fractions for the friction velocity of $0.5\,\mathrm{m\,s^{-1}}$ corresponding to the last segments of the AD channel. Besides, as it can be seen in Fig. 10(c), this additional uncertainty on the last segments (with average friction velocities of $0.5\,\mathrm{m\,s^{-1}}$) does not affect the determination of the median resuspension fractions for the four particle size bins studied. Hence, taking into account the friction velocity map established by numerical simulations in Section 3.1 (Fig. 8), each of the ten segments of 4×12 mm^2 can be associated with an average friction velocity and its standard deviation. It is thus possible to express the resuspension fraction measured in a particular area along the channel of the AD according to the average friction velocity specific of that area. These transformations are given in Fig. 10(c) where the mean resuspension fractions (with their corresponding standard deviations) are represented as a function of the average friction velocity for the four size bins studied. It should also be noted that the choice of dividing the particle deposit into 10 segments comes from a compromise between the need to have enough particles to count in each segment, a good coverage of the different velocity zones in the channel of the AD and a manageable number of measurements to be carried out. For instance, increasing the number of segments would imply more precision as for the evolution of the resuspension fraction according to friction velocity but the drawback is a lower number of particles in each segment resulting in an increased error on the resuspension fraction. A more detailed analysis about the influence of segmentation on data analysis is proposed in Section S2 of the supplementary materials.

3.5. Tritiated tungsten particles

The same methodology has been followed with radioactive tungsten particles containing tritium. Making of the deposits and resuspension experiments are identical to previous tests with the non-radioactive powder but were realized in a nuclear glove box and optical microscopy analysis was performed with the same apparatus in a confined laboratory. A detailed procedure describing the loading of the particles with tritium can be found in Bernard et al. (2019), El-Kharbachi et al. (2014), Peillon et al. (2020). The labeling of the tungsten particles with tritium is based on a gas adsorption/diffusion procedure at high temperature. The tungsten powder is exposed to a pure tritium atmosphere at 743 K for 2 h. The diffusion mechanism is then thermally quenched by dropping the glass vial which contains the powder into liquid nitrogen. After the loading procedure tritium desorption is monitored. The tritiated powder is recovered after several days until reaching a plateau in the cumulated amount of desorbed tritium. The inventory of tritium retained in the particle is then measured after full dissolution and liquid scintillation counting. For the micrometer spherical tungsten particles used in this study the tritium trapped activity is around $100\,\mathrm{MBq\,g^{-1}}$. Such activity is quite low compared to the one obtained for sub-micrometer tungsten particles ($>10\,\mathrm{GBq\,g^{-1}}$) having much higher specific surface areas. The reader interested in a more detailed analysis is invited to consult our previous work (Peillon et al., 2020). Resuspension data obtained with a tritiated tungsten powder are depicted in Fig. 11 in the same way as before for non-radioactive tungsten particles.

4. Discussion

4.1. Threshold friction velocities and median adhesion forces

From the results obtained with the resuspension experiments reported in Fig. 10(c) and Fig. 11, it is possible to identify a friction velocity threshold ($u_\star^{\mathrm{th}}$) i.e. the friction velocity for which 50% of the particles are removed. To do that, it is common to fit the data with a continuous distributions. Most of the time the detachment parameter (which depends on the method used) of real systems is approximated by either a log-normal distribution, often used with broad particle size distribution and rough surfaces (Brambilla et al., 2017; Ilse et al., 2020), or Weibull distribution when surfaces are smooth and the particle size distribution is narrow (Götzinger & Peukert, 2004). For the present case where a smooth glass surface is used in combination with spherical particles having a narrow size distribution, the Weibull law is best suited. In order to simplify the calculations, the particle size bins are represented by their

Table 3
Threshold friction velocities $u_\star^{th}$ and median adhesion force F_{50} obtained for the non-radioactive tungsten particles and the tritiated tungsten particles with the aerodynamic method.

	Median diameter	11 µm	13 µm	15 µm	17 µm
Non-radioactive	$u_\star^{th}$ (m s^{-1})	1.12 ± 0.20	0.95 ± 0.11	0.82 ± 0.10	0.69 ± 0.07
	F_{50} (nN)	211 ± 35	223 ± 24	233 ± 26	231 ± 22
Tritiated	$u_\star^{th}$ (m s^{-1})	0.98 ± 0.30	0.91 ± 0.24	0.81 ± 0.17	0.75 ± 0.15
	F_{50} (nN)	183 ± 53	213 ± 55	230 ± 48	252 ± 47

median diameters, namely 11 µm, 13 µm, 15 µm and 17 µm. For a positive random friction velocity $u_\star > 0$, its Weibull cumulative distribution function (CDF) is expressed by:

$$f\left(u_\star, \lambda, k\right) = 1 - e^{-\left(u_\star/\lambda\right)^k}, \tag{21}$$

where $k > 0$ is the shape parameter and $\lambda > 0$ is the scale parameter of the distribution. The threshold friction velocity value is easily obtained using the median of the Weibull distribution which is written $u_\star^{th} = \lambda\,(\ln 2)^{1/k}$. Moreover, the variance σ^2 of the distribution is expressed by $\sigma^2 = \lambda^2\Gamma\left(1+\frac{2}{k}\right) - \overline{u_\star}^2$ with $\overline{u_\star} = \lambda\Gamma\left(1+\frac{1}{k}\right)$ the mean of the distribution, Γ being the gamma function. The fitting of the Weibull distributions over the mean resuspension fractions $\overline{\mathrm{KR}_i}$ for each median diameter i are reported in the graphics of Fig. 10(c) for the non-radioactive particles and Fig. 11 for the tritiated particles. The same methodology employed in Section 2.4 to take into account the experimental variation of the resuspension fractions SD_i is applied and two additional Weibull distributions are plotted on the graphics. Therefore, two additional median friction velocities corresponding to a lower and an upper value of the threshold friction velocity can be calculated. The friction velocity thresholds and their relative errors (twice the standard deviation between the median, lower and upper values of the friction velocity thresholds) are gathered in Table 3. The parameters of the corresponding Weibull distributions are reported in Table S2 of the supplementary materials. For each diameter it can be noted that the values of the threshold friction velocities are substantially equivalent for the two populations of particles, whether they are radioactive or not, considering the uncertainty on the determination of the friction velocity thresholds. Notice that for the tritiated particles with 11 µm median diameter a rather large dispersion of resuspension fractions was obtained, leading to a smaller friction velocity threshold and an increased uncertainty. Using the moment-balance model introduced in Section 1 by Eq. (1), it is possible to use the threshold friction velocities to estimate the median adhesion force F_{50} (here only van der Waals forces are considered) for a given particle diameter. The lever-arm a is here taken as the radius of contact given by the JKR theory in Eq. (8) and derived using the data reported in Table 1. Note that the model used in Eq. (1) is rather sensitive to the choice of this lever-arm distance as recently discussed by Brambilla and Brown (2020) for the case of rough surfaces. However, without additional information on the asperity radius distribution and surface coverage, a mean value of $R_p/a \approx 40$ (for the particle sizes investigated) is used for the calculation. The results of these calculation are also reported in Table 3.

4.2. Comparing AM and AFM results

The LN distributions describing the adhesion forces measured by AFM and the medians and standard deviations of the Weibull distributions describing the adhesion forces of radioactive and non-radioactive W particles measured by the AM are compared in Fig. 12. Note that the AFM distributions are represented by box-plots which display the datasets based on six numbers: the minimum value, the first and third quartiles, the median and mean of the distribution and the maximum value. It should also be noted that only particles of 15 µm in diameter were studied with the two techniques, the other two sizes of particles studied by AFM being either smaller (7 µm in diameter) or larger (20 µm in diameter). For the 15 µm diameter particles, a very good agreement is observed between the two techniques, the median adhesion force measured by AFM being 223±75 nN while the one measured with the AM is 233±26 nN for non-radioactive particles. These results show the relevance of the experimental methodology used with the aerodynamic device to deduce the adhesion forces of particles in a monolayer deposit. To the author's knowledge, such a detailed comparison between the two experimental techniques (AFM and AM) is a first of its kind and allows to validate the AM developed in this study for indirect adhesion measurements. Indeed the good agreement between the two experimental methods indicates that repeating AFM adhesion measurements with one particle over thousands locations is, in the end, equivalent to perform one measurement with thousands particles of the same size but randomly distributed on the surface. Moreover, it has been demonstrated that the use of a simple force balance model such as that given by Eq. (1) makes it possible to deduce the median adhesion forces of a population of particles from their resuspension fractions and from the aerodynamic conditions inside the AD only. Indeed, the use of an AFM is not possible in all situations (significant experimental effort, handling of toxic or radioactive products, significant surface roughness) whereas the proposed AM is easy to implement at the condition of knowing the friction velocities in the channel of the device and of having an optical microscope to count the particles. Thus, the *rms* surface roughness as well as the Hamaker constants do not need to be known to evaluate the median adhesion forces of the particles since they are integrated in the resuspension fractions measured. This last point is addressed in the next paragraph where the results obtained with the AM are directly compared with the adhesion force models presented in Section 1. Among these, the model of Rabinovich et al. (2000b), which take into account the *rms* roughness of the surface, manages to reproduce very well the experimental data obtained regardless of the measurement technique used.

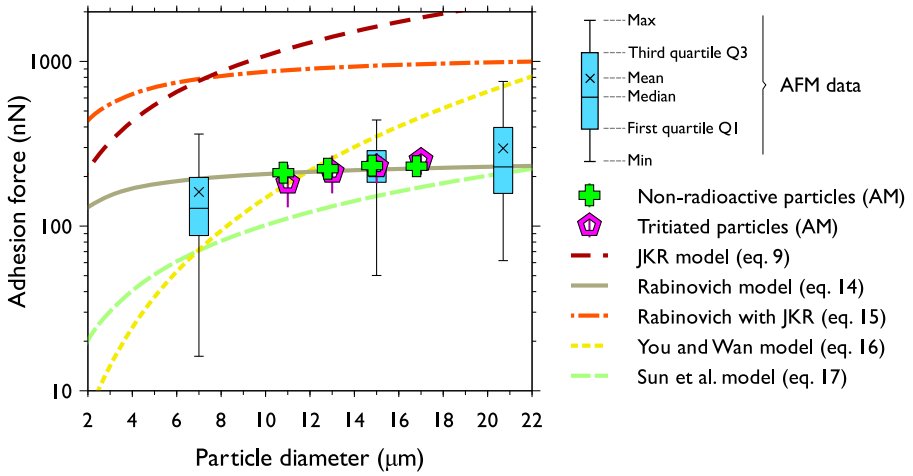

Fig. 12. Comparison between the AFM data, the adhesion forces obtained with the aerodynamic method (AM) for both tritiated and non-radioactive particles and different adhesion models.

4.3. Comparison with adhesion force models

The JKR model (Eq. (9)) and both formulations of the Rabinovich et al. (2000a) model, i.e. considering non-deformable objects (Eq. (14)) or including the JKR theory at the contact point (Eq. (15)) are reported in Fig. 12 with respect to the particle's diameter. In addition the JKR-based models of You and Wan (2013) and the more recent one of Sun et al. (2021) are also given. These models consider surface roughness via a correction coefficient accounting for the reduced contact area between the particle and rough surface. With the present adhesion datasets it can be seen that the conventional JKR model fails to predict the adhesion forces observed giving values more than one order of magnitude above the experimental results. Moreover, its linear dependency with respect to the size of the particle implies a constant increase of the adhesion force which is not representative of the evolution observed even with a smooth surface such as glass having nanometric roughness. On the other hand, the model of Rabinovich et al. (2000b) considering non-deformable objects faithfully reproduces experimental data using only few parameters namely, the effective Hamaker constant $A^{\text{eff}}_{\text{W/SiO}_2} = 16 \times 10^{-20}$ J, the minimal distance of contact $z_0 = 0.3$ nm, the average $rms = 2.2$ nm roughness and the average peak-to-peak distance $\lambda_s = 320$ nm. In addition, the median adhesion forces obtained with the AM for radioactive and non-radioactive W particles overlap well with the AFM data and are well captured by the model (Eq. (14)). We emphasize on the fact that experimental results obtained with the aerodynamic method are perfectly represented by the model for all the particle sizes tested. Moreover, median adhesion forces given by the AFM measurements agree well with the model and the aerodynamic experiments for the two largest particle diameters used, namely, 15 μm and 21 μm. For the smaller 7 μm diameter particle, the median adhesion force (143.5 ± 58 nN) is slightly lower than the one given by the model (199 nN) although of the same order of magnitude. On the contrary, the JKR-based model derived by Rabinovich et al. (2000a) fails to describe the experimental data giving values five times greater although the trend is somehow respected. To complete the comparison, it can be noticed that both JKR-based models of You and Wan (2013) and Sun et al. (2021) give adhesion force values of same order of magnitude as the AFM data. While the first shows a rapid increase in adhesion force with particle size (a value around 750 nN is given for the 20.7 μm diameter particle), the second model succeeds in capturing some values of the experimental force distributions for the three particle sizes studied but still remaining below the experimental values. For the calculation with the Sun et al. (2021) model, the adjusting parameter $k_A = 1.6$ was considered.

4.4. Accounting for the rms roughness distribution

The previous comparison highlighted the relevance of the Rabinovich et al. (2000b) model to describe the experimental results. However, the computation of the adhesion force was realized using the mean *rms* roughness of the glass surface. In Section 2.2 we showed that the microparticles deposited on such a surface will rather experience a distribution of the *rms* roughness depending on their location on the surface. Indeed, at the scale of the contact surface area between the particle and the substrate we demonstrated that the *rms* of the substrate follows a log-normal distribution with parameters $\mu = 0.75$ and $\sigma = 0.26$. Thus, for each location, the van der Waals interaction derived by the adhesion model will depend on the local *rms* roughness and overall, the adhesion force for a specific particle diameter over the entire surface will follow the same probabilistic distribution as the *rms* roughness. Thus, for a particle diameter D_p and a random *rms* value $x > 0$, its adhesion force distribution $F_{adh}(x, \mu, \sigma)$ can be written as:

$$F_{adh}(x, \mu, \sigma) = \int_{x_{min}}^{x_{max}} f_{adh}(x) \times f_{rms}(x, \mu, \sigma)\, dx, \tag{22}$$

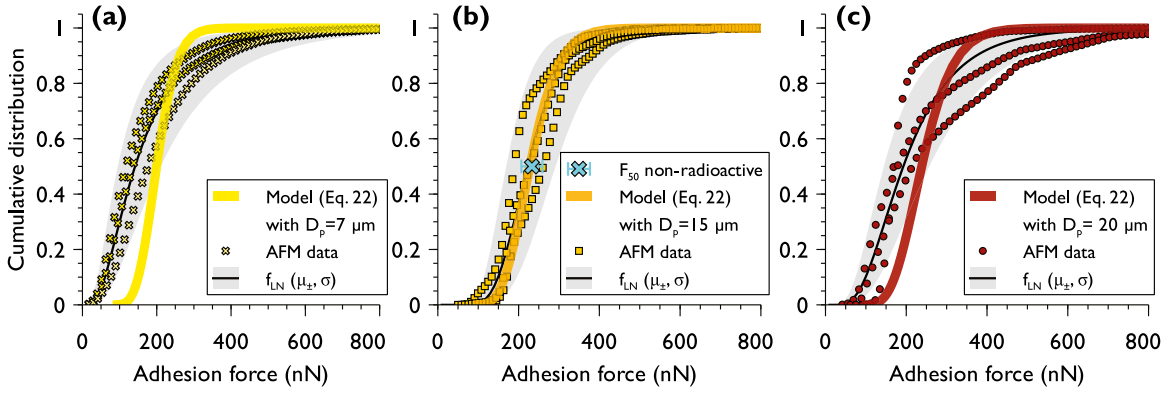

Fig. 13. AFM data from Fig. 5 compared to cumulative distributions of adhesion forces using the model given by Eq. (22) for particle diameters of 7 µm **(a)**, 15 µm **(b)** and 20 µm **(c)**.

where f_{rms} is the CDF of the LN distribution describing the *rms* roughness and expressed by Eq. (19). The model given by Eq. (22) has been derived for $x_{min} = 0.1$ nm, $x_{max} = 5$ nm and $dx = 0.1$ nm and for three particle diameters: 7 µm, 15 µm and 20 µm. The corresponding cumulative distributions are presented in Figs. 13(a)–13(c), respectively. It shows that, as the particle size increases, the cumulative distributions of adhesion forces given by Eq. (22) shift toward larger force values. Likewise, the dispersion of the adhesion force distributions increases with the particle size. On the three particle sizes tested with the AFM, we note that the proposed analytical model gives a perfect description of the distribution of the adhesion forces obtained for the 15 µm diameter particle only. Similarly, the median value (F_{50}) of adhesion forces obtained with the aerodynamic method for this particle size is in very good agreement with the model. On the other hand we find discrepancies both on the median values and the spread of the cumulative distributions between the data and the model for the other two particle sizes. Indeed, for the 7 µm and 20 µm diameter particles, the analytical model gives higher values of median adhesion forces and fails to capture extreme values (low and high) of the measured force distributions. This last point is interesting and shows that the approach used here, considering only the *rms* parameter of the substrate, requires a more refined description of the surface roughness features (size distribution, radius of curvature and peak-to-peak distances) as suggested by Henry and Minier (2018). In addition, future work should characterize the roughness features of the surface of the particle itself since it can also influence the area of contact with the substrate.

4.5. Influence of tritium beta decay on the adhesion

4.5.1. Assessing the magnitude of the electrostatic image force

Following the results presented in Fig. 12 showing a very small difference between the adhesion forces of non-radioactive and tritiated tungsten particles, we propose in this paragraph to estimate by calculation the value of the electrostatic image force attributable to self-charging. Indeed, the median adhesion forces found for the two populations of particles are very close and can be considered identical taking into account the experimental errors. To assess the contribution of the electrostatic image force given by Eq. (18) let us consider a 17 µm diameter tungsten particle with a specific activity in tritium of 100 MBq g^{-1}. We first need to estimate its electrostatic charge due to the tritium loading. In a previous work we have used a Monte Carlo method to calculate the self-charging rate m of such tungsten particle assuming that a layer of tungsten tri-oxide (WO_3) with a few tens of nanometers thickness surrounds the metal core of the particle (Peillon et al., 2020). For such a particle we found a self-charging rate of $m = 0.84$ s^{-1}, i.e., the particle acquires 0.84 electrical charge every second. If the particle is in absolute vacuum, the electrostatic charging would continue until self-generated field at the surface of the particle reaches the value required for spontaneous emission of electrons from its surface. This corresponds to the saturation charge of a solid particle which expression can be found in Hinds (1999). But in normal atmospheric conditions two neutralization phenomena will limit the electrostatic charging: (i) the self-generated ionic cloud which is determined by the range of the beta radiation and (ii) the ionic background concentration due to cosmic rays and natural radiation that ranges between 10^8–10^9 m^{-3} (Clement & Harrison, 1992). To facilitate the assessment, we will consider only negative ions in the following calculations since the particle is assumed positively charged (electrons coming from the β-decay of tritium exit the particle thus leaving a positive charge). This assumption maximize the estimation of the number of negative ions created by the β-decays coming from the particle and which can backscatter onto the particle and neutralize it. We will see that, taking into account the low number of ions created from the decays of tritium compared to the concentration of natural ions, this hypothesis can indeed be applied in our case. The total concentration of negative ions around the particle is thus $N_- = n_- + n_{b-}$ where n_- is the ion concentration produced by the exiting β-radiations from the particle and n_{b-} the ion background concentration. If we consider a single isolated particle in air, the ion concentration from β-radiation is given by $n_- = \left(I_\beta m/\alpha_i\right)^{1/2}$ where $I_\beta = E_{\max}/3w_i$ is the ion-pair production constant, $\alpha_i = 1.6\times10^{-12}$ m^3 s^{-1} the ion–ion recombination coefficient, $E_{\max} = 18.6$ keV the maximum energy of the tritium β-decay (Bé et al., 2010) and $w_i = 34$ eV the mean energy required to form an ion pair in ambient air (Gensdarmes et al., 2001). With these values, we found an ion-pair production constant $I_\beta = 182$ i.p.decay^{-1} and an ion concentration from β-radiation

$n_- \approx 10^7$ m^{-3}. In this calculation we have neglected the particular geometry of the system by considering that the particle is airborne. The presence of the surface will have the effect of further reducing the formation of ions by beta radiation coming from the particle since the energy of the emitted decay products is dissipated in the surface rather than by creating ion pairs in the surrounding gas (Clement & Harrison, 2000). The total ion concentration N_- is thus governed by the natural background ion concentration which is one to two orders of magnitude above the ion concentration from the beta radiation exiting the particle. The mean number of charge unit J acquired by a β-decaying particle at steady state is given by (Clement & Harrison, 1992):

$$J = \frac{m\epsilon_0}{e\mu_- N_-}, \tag{23}$$

where $\mu_- = 1.25 \times 10^{-4}$ m^2 V^{-1} s^{-1} (Mohnen, 1976) is the negative ion mobility at standard conditions. Using Eq. (23) with our case study, one find a mean number of elementary charges carried by a 17 µm particle between $368 < J < 3385$ depending on the background ion concentration chosen for the calculation. Assuming an homogeneous distribution of charges at the particle's surface, this yields a mean surface charge density of 0.26–2.6 µC m^{-2}. Knowing the equilibrium charge state of the particle, we can now derive its electrostatic adhesion force using Eq. (18) with $\alpha \approx 4$ to account for the polarization of the dielectric tungsten particle (Peillon et al., 2020) and a relative permittivity $\kappa_s = 5$ for the glass substrate which will reduce by a factor of 2/3 the magnitude of the image charge $Q' = \frac{2}{3}Q$ in the glass substrate. We thus find very low values for the electrostatic adhesion forces comprised between 0.3 pN and 25 pN depending on the ion concentration conditions near the particle. Comparing with the van der Waals force given by the adhesion models used previously it can be seen that the electrostatic contribution arising from self-charging is by far negligible in the adhesion for the present case. Nonetheless, we recall here that the tritium specific activity of the tungsten particles used in this study is relatively low compared to the tritium specific activities measured in other tungsten powders, e.g. 3.4 GBq g^{-1} for commercial metallurgy tungsten powder (Bernard et al., 2016) or above 10 GBq g^{-1} for tungsten nanoparticles (El-Kharbachi et al., 2014). Consequently, for greater tritium loads, a higher self-charging rate is expected yielding more charge accumulation on the particle's surface. Moreover, in a vacuum environment the neutralization by atmospheric ions is removed thus allowing build-up of electric charges onto radioactive particles. This scenario has been examined in our previous study (Peillon et al., 2020) where we estimated that the electrostatic image force on a 17 µm diameter tritiated tungsten particle could reach 10 nN in 17 h thus exceeding the magnitude of van der Waals forces after few days.

4.5.2. Consideration of uncertainty sources

To complete the discussion on the very low values given by the calculation of the electrostatic image force, we propose to address here the impact of the various assumptions that have been made in the previous paragraph and which may induce an underestimation of the image force. Indeed, we have considered that the charge surface density is homogeneously distributed on the particle's surface which is rarely the case for real systems. For example Kim et al. (2014) have explicitly shown patch charge domains on ceramic-like material loaded with ^{137}Cs by means of electrical atomic force microscopy measurements. This stems from various reasons such as material's defects which will enhance radionuclide trapping in certain locations as shown recently by Alimov et al. (2021) for tritium trapping in tungsten. The influence of patch charge areas on a dielectric particle have been studied by Feng and Hays (1998), Techaumnat and Kadonaga (2011) who showed an increase in adhesion by several times due to the increase of the polarization of the particle. Polarization is indeed an important factor which also depends on the relative permittivity of the materials which can increase the electrostatic adhesion force up to two orders of magnitude according to Matsuyama and Yamamoto (1998). Finally, it can be noticed here that, as with the van der Waals forces, the electrostatic forces will also be influenced by the roughness of the surface. On the other hand, the increase in roughness is systematically to the detriment of the van der Waals forces, the latter acting at very short distances while the electrostatic forces retain their influence over much greater distances (Gady et al., 1996). This feature has been explored recently by Rajupet et al. (2021) showing that the electrostatic adhesion force is indeed dependent of the surface roughness (and can be either enhanced or diminished depending on the surface roughness parameters and the size of the particle) but is much less sensitive to it compared to the van der Waals forces. In the configurations that we have studied in this work ($R_p \gg \lambda_s$), and although we have shown that the measured van der Waals forces are at least an order of magnitude lower than those of the theoretical case of atomically flat surfaces, the low roughness of the glass substrate and the large particle sizes favors the action of intermolecular forces over electrostatic forces. Obviously, this balance of forces is likely to be greatly modified in the presence of an external electric field, which can be encountered in various processes or conditions (Feng & Hays, 2003; Matsusaka et al., 2015; Takeuchi, 2006; Tolias et al., 2016), or by a significant surface roughness which would generate a drastic decrease in the van der Waals forces (Cheng et al., 2002; Götzinger & Peukert, 2004; Peillon et al., 2019).

5. Conclusion

We have presented in this study an experimental aerodynamic method to deduce the adhesion forces of micrometric tungsten particles deposited on a glass surface. This method is based on the use of a device allowing dust sampling as well as laboratory experiments. Thanks to the numerical simulation of the air flows produced by the device, we have shown that it is possible to go back to the adhesion forces of the particles from the first principle. In order to validate this approach, we carried out a detailed study of the adhesion forces with the chosen particle/surface system using atomic force microscopy. The good agreement between the values found with the two experimental methods indicates that the procedure implemented with the aerodynamic device is reliable and can be used to obtain median adhesion forces for various particle/surface systems including toxic or radioactive samples. Indeed, we were able to deploy this type of measurement in a nuclearized glove box to study the resuspension of tungsten particles loaded

with tritium in order to deduce their adhesion forces. In addition, we have shown that the experimental adhesion forces obtained are well described by the analytical model of Rabinovich et al. (2000b) which considers the *rms* roughness of the surface. On this occasion, we showed that the distribution of the *rms* roughness of the surface can be approximated by a continuous probability distribution which can then be integrated in the adhesion force model in order to take into account the dispersion of the *rms* roughness distribution in the adhesion force calculations. Such a feature emphasize the importance of roughness characterization when performing resuspension experiments and modeling as it extends the validity of theoretical models which generally only consider the average *rms* roughness of surfaces. Beyond the validation of the AM with the AFM force measurements, the results obtained in this study show that the complementarity of the two techniques appeal for in-depth analysis of the resuspension phenomenon and future experimental works should be devoted to the improvement and validation of resuspension models. As we saw in Section 2, AFM allows to obtain a detailed description of the surface topography where other parameters than the mean *rms* roughness can be extracted, in particular the distribution of curvature radii of asperities and their surface coverage. Moreover, particle/surface adhesion force distributions measured by AFM can be directly injected in resuspension models, thus taking into account extreme values of adhesion forces that are not depicted by simple log-normal distributions and can influence long-term resuspension. On the other hand, the experiments carried out with radioactive particles did not show any significant differences compared to non-radioactive particles concerning their median adhesion forces via a contribution of the electrostatic image force. During the discussion, we addressed the different aspects that can penalize the highlighting of such a contribution. In particular, the low specific activity in tritium of the tungsten particles, the low roughness of the substrate as well as the neutralization of the charges by the natural ions in the vicinity of the particles lead to very low values of electrostatic image forces. New experiments with broader particle size distributions and other surfaces are planned to extend the validity range of the aerodynamic method. Furthermore, it is being considered to use Kelvin Probe Force Microscopy (KPFM) to measure the charge state of individual radioactive metallic particles having higher tritium specific activity than the ones used in the present work. Such type of measurements would allow to test the hypothesis proposed on the self-charging and neutralization mechanisms for the particle/surface system studied.

Declaration of competing interest

The authors declare that they have no known competing financial interests or personal relationships that could have appeared to influence the work reported in this paper.

Acknowledgments

The authors wish to thank Mr. Sébastien Garcia-Argote (CEA/IRFM) for his invaluable help in carrying out the glove box experiments with the radioactive samples. Likewise, our sincere thanks go to Mr. Siddharth Rajupet (Case Western Reserve University) for his assistance in writing the MATLAB subroutine to obtain the *rms* roughness distribution of the substrate from the AFM data.

Appendix A. Supplementary data

Supplementary material related to this article can be found online at https://doi.org/10.1016/j.jaerosci.2022.106037.

References

Alimov, V., Torikai, Y., Hatano, Y., & Schwarz-Selinger, T. (2021). Tritium retention in displacement-damaged tungsten exposed to deuterium-tritium gas mixture at elevated temperatures. *Fusion Engineering and Design*, *162*, Article 112100. http://dx.doi.org/10.1016/j.fusengdes.2020.112100.

Alvo, S., Lambert, P., Gauthier, M., & Régnier, S. (2010). A van der Waals force-based adhesion model for micromanipulation. *Journal of Adhesion Science and Technology*, *24*, 2415–2428. http://dx.doi.org/10.1201/b12181-7.

Balden, M., Endstrasser, N., Humrickhouse, P., Rohde, V., Rasinski, M., von Toussaint, U., Elgeti, S., Neu, R., & the ASDEX Upgrade Team (2014). Collection strategy, inner morphology, and size distribution of dust particles in ASDEX upgrade. *Nuclear Fusion*, *54*, Article 073010. http://dx.doi.org/10.1088/0029-5515/54/7/073010.

Banari, A., Henry, C., Fank Eidt, R. H., Lorenz, P., Zimmer, K., Hampel, U., & Lecrivain, G. (2021). Evidence of collision-induced resuspension of microscopic particles from a monolayer deposit. *Physical Review Fluids*, *6*, L082301. http://dx.doi.org/10.1103/PhysRevFluids.6.L082301.

Baron-Wiechec, A., Fortuna-Zaleśna, E., Grzonka, J., Rubel, M., Widdowson, A., Ayres, C., Coad, J. P., Hardie, C., Heinola, K., & Matthews, G. F. (2015). First dust study in JET with the ITER-like wall: sampling, analysis and classification. *Nuclear Fusion*, *55*, Article 113033. http://dx.doi.org/10.1088/0029-5515/55/11/113033.

Barth, T., Reiche, M., Banowski, M., Oppermann, M., & Hampel, U. (2013). Experimental investigation of multilayer particle deposition and resuspension between periodic steps in turbulent flows. *Journal of Aerosol Science*, *64*, 111–124. http://dx.doi.org/10.1016/j.jaerosci.2013.04.011.

Bé, M.-M., Chisté, V., Dulieu, C., Mougeot, X., Browne, E., & Chechev, V. (2010). *Monographie BIPM-5: vol. 1–5, Table of radionuclides (comments on evaluation)*. Sèvres: Bureau International des Poids et Mesures.

Beach, E., Tormoen, G., Drelich, J., & Han, R. (2002). Pull-off force measurements between rough surfaces by atomic force microscopy. *Journal of Colloid and Interface Science*, *247*, 84–99. http://dx.doi.org/10.1006/jcis.2001.8126.

Benito, J., Aracena, K., Uñac, R., Vidales, A., & Ippolito, I. (2015). Monte Carlo modelling of particle resuspension on a flat surface. *Journal of Aerosol Science*, *79*, 126–139. http://dx.doi.org/10.1016/j.jaerosci.2014.10.006.

Bernard, E., Delaporte, P., Jambon, F., Rousseau, B., Grisolia, C., Chaudanson, D., & Nitsche, S. (2016). Tungsten dust in fusion tokamaks: relevant dust laser production, characterization and behaviour under tritium loading. *Physica Scripta*, *T167*, Article 014071. http://dx.doi.org/10.1088/0031-8949/t167/1/014071.

Bernard, E., Sakamoto, R., Hodille, E., Kreter, A., Autissier, E., Barthe, M.-F., Desgardin, P., Schwarz-Selinger, T., Burwitz, V., Feuillastre, S., Garcia-Argote, S., Pieters, G., Rousseau, B., Ialovega, M., Bisson, R., Ghiorghiu, F., Corr, C., Thompson, M., Doerner, R., ... Grisolia, C. (2019). Tritium retention in W plasma-facing materials: Impact of the material structure and helium irradiation. *Nuclear Materials and Energy*, *19*, 403–410. http://dx.doi.org/10.1016/j.nme.2019.03.005.

Biasi, L., de los Reyes, A., Reeks, M., & de Santi, G. (2001). Use of a simple model for the interpretation of experimental data on particle resuspension in turbulent flows. *Aerosol Science*, 1175–1200.

Boor, B. E., Siegel, J. A., & Novoselac, A. (2013). Monolayer and multilayer particle deposits on hard surfaces: Literature review and implications for particle resuspension in the indoor environment. *Aerosol Science and Technology*, *47*, 831–847. http://dx.doi.org/10.1080/02786826.2013.794928.

Braaten, D., Paw U, K., & Shaw, R. (1990). Particle resuspension in a turbulent boundary layer-observed and modeled. *Journal of Aerosol Science*, *21*, 613–628. http://dx.doi.org/10.1016/0021-8502(90)90117-G.

Brambilla, S., & Brown, M. J. (2020). Impact of the adhesion-force lever-arm "a" on the Rock 'n' Roll resuspension model and how to compute it from contact mechanics. *Journal of Aerosol Science*, *143*, Article 105525. http://dx.doi.org/10.1016/j.jaerosci.2020.105525.

Brambilla, S., Speckart, S., & Brown, M. J. (2017). Adhesion and aerodynamic forces for the resuspension of non-spherical particles in outdoor environments. *Journal of Aerosol Science*, *112*, 52–67. http://dx.doi.org/10.1016/j.jaerosci.2017.07.006.

Butt, H.-J., Cappella, B., & Kappl, M. (2005). Force measurements with the atomic force microscope: Technique, interpretation and applications. *Surface Science Reports*, *59*, 1–152. http://dx.doi.org/10.1016/j.surfrep.2005.08.003.

Cheng, W., Dunn, P. F., & Brach, R. M. (2002). Surface roughness effects on microparticle adhesion. *Journal of Adhesion*, *78*, 929–965. http://dx.doi.org/10.1080/00218460214510.

Chung, E., Yiacoumi, S., Lee, I., & Tsouris, C. (2010). The role of the electrostatic force in spore adhesion. *Environmental Science and Technology*, *44*, 6209–6214. http://dx.doi.org/10.1021/es101730y.

Clement, C., Calderbank, D., & Harrison, R. (1994). Radioactive aerosol charging with spatially varying ion concentrations. *Journal of Aerosol Science*, *25*, 623–637. http://dx.doi.org/10.1016/0021-8502(94)90004-3.

Clement, C., & Harrison, R. (1991). Self-charging of radioactive aerosols. *Journal of Aerosol Science*, *22*, S175–S178. http://dx.doi.org/10.1016/S0021-8502(05)80063-1.

Clement, C., & Harrison, R. (1992). The charging of radioactive aerosols. *Journal of Aerosol Science*, *23*, 481–504. http://dx.doi.org/10.1016/0021-8502(92)90019-R.

Clement, C., & Harrison, R. (2000). Enhanced localized charging of radioactive aerosols. *Journal of Aerosol Science*, *31*, 363–378. http://dx.doi.org/10.1016/S0021-8502(99)00064-6.

Das, S., Sreeram, P. A., & Raychaudhuri, A. K. (2007). A method to quantitatively evaluate the Hamaker constant using the jump-into-contact effect in atomic force microscopy. *Nanotechnology*, *18*, Article 035501. http://dx.doi.org/10.1088/0957-4484/18/3/035501.

Dejeu, J., Bechelany, M., Philippe, L., Rougeot, P., Michler, J., & Gauthier, M. (2010). Reducing the adhesion between surfaces using surface structuring with PS latex particle. *ACS Applied Materials & Interfaces*, *2*, 1630–1636. http://dx.doi.org/10.1021/am100156c.

Derjaguin, B., Muller, V., & Toporov, Y. (1975). Effect of contact deformations on the adhesion of particles. *Journal of Colloid and Interface Science*, *53*, 314–326. http://dx.doi.org/10.1016/0021-9797(75)90018-1.

Dougniaux, G., Sow, M., Peillon, S., Grisolia, C., & Gensdarmes, F. (2019). Monte-Carlo simulations of electrostatic self-charging of tritiated tungsten and beryllium particles. *Journal of Physics: Conference Series*, *1322*, Article 012027. http://dx.doi.org/10.1088/1742-6596/1322/1/012027.

Ducker, W. A., Senden, T. J., & Pashley, R. M. (1991). Direct measurement of colloidal forces using an atomic force microscope. *Nature*, *353*, 239–241.

El-Kharbachi, A., Chêne, J., Garcia-Argote, S., Marchetti, L., Martin, F., Miserque, F., Vrel, D., Redolfi, M., Malard, V., Grisolia, C., & Rousseau, B. (2014). Tritium absorption/desorption in ITER-like tungsten particles. *International Journal of Hydrocarbon Engineering*, *39*, 10525–10536. http://dx.doi.org/10.1016/j.ijhydene.2014.05.023.

Feng, J., & Hays, D. (1998). A finite-element analysis of the electrostatic force on a uniformly charged dielectric sphere resting on a dielectric-coated electrode in a detaching electric field. *IEEE Transactions on Industry Applications*, *34*, 84–91. http://dx.doi.org/10.1109/28.658725.

Feng, J. Q., & Hays, D. A. (2003). Relative importance of electrostatic forces on powder particles. *Powder Technology*, *135–136*, 65–75. http://dx.doi.org/10.1016/j.powtec.2003.08.005.

Figgis, B., Ennaoui, A., Ahzi, S., & Rémond, Y. (2017). Review of PV soiling particle mechanics in desert environments. *Renewable and Sustainable Energy Reviews*, *76*, 872–881. http://dx.doi.org/10.1016/j.rser.2017.03.100.

Fillingham, P., Kottapalli, K., Zhan, X., & Novosselov, I. V. (2019). Characterization of adhesion force in aerodynamic particle resuspension. *Journal of Aerosol Science*, *128*, 89–98. http://dx.doi.org/10.1016/j.jaerosci.2018.11.006.

Gady, B., Schleef, D., Reifenberger, R., Rimai, D., & DeMejo, L. P. (1996). Identification of electrostatic and van der Waals interaction forces between a micrometer-size sphere and a flat substrate. *Physical Review B*, *53*, 8065–8070. http://dx.doi.org/10.1103/PhysRevB.53.8065.

Gan, Y. (2007). Invited review article: A review of techniques for attaching micro- and nanoparticles to a probe's tip for surface force and near-field optical measurements. *Review of Scientific Instruments*, *78*, Article 081101. http://dx.doi.org/10.1063/1.2754076.

Gelain, T., Gensdarmes, F., Peillon, S., & Ricciardi, L. (2020). CFD modelling of particle resuspension in a toroidal geometry resulting from airflows during a loss of vacuum accident (LOVA). *Fusion Engineering and Design*, *151*, Article 111386. http://dx.doi.org/10.1016/j.fusengdes.2019.111386.

Gensdarmes, F., Boulaud, D., & Renoux, A. (2001). Electrical charging of radioactive aerosols comparison of the Clement Harrison models with new experiments. *Journal of Aerosol Science*, *32*, 1437–1458. http://dx.doi.org/10.1016/S0021-8502(01)00065-9.

Götzinger, M., & Peukert, W. (2004). Particle adhesion force distributions on rough surfaces. *Langmuir*, *20*, 5298–5303. http://dx.doi.org/10.1021/la049914f.

Gradoń, L. (2009). Resuspension of particles from surfaces: Technological, environmental and pharmaceutical aspects. *Advanced Powder Technology*, *20*, 17–28. http://dx.doi.org/10.1016/j.apt.2008.10.009.

Grisolia, C., Gensdarmes, F., Peillon, S., Dougniaux, G., Bernard, E., Autricque, A., Pieters, G., Rousseau, B., Feuillastre, S., Garcia-Argote, S., Carvalho, O., Malard, V., George, I., Lebaron-Jacobs, L., Orsiere, T., Uboldi, C., Rose, J., Sanles Sobrido, M., Lambertin, D., ... Dinescu, G. (2019). Current investigations on tritiated dust and its impact on tokamak safety. *Nuclear Fusion*, *59*, Article 086061. http://dx.doi.org/10.1088/1741-4326/ab1a76.

Guingo, M., & Minier, J.-P. (2008). A new model for the simulation of particle resuspension by turbulent flows based on a stochastic description of wall roughness and adhesion forces. *Journal of Aerosol Science*, *39*, 957–973. http://dx.doi.org/10.1016/j.jaerosci.2008.06.007.

Hamaker, H. (1937). The London—van der Waals attraction between spherical particles. *Physica*, *4*, 1058–1072. http://dx.doi.org/10.1016/S0031-8914(37)80203-7.

Hays, D. A., & Sheflin, J. C. (2005). Electrostatic adhesion of ion and triboelectric-charged particles. *Journal of Electrostatics*, *63*, 687–692. http://dx.doi.org/10.1016/j.elstat.2005.03.031, 10th international conference on electrostatics.

Henry, C., & Minier, J.-P. (2014). Progress in particle resuspension from rough surfaces by turbulent flows. *Progress in Energy and Combustion Science*, *45*, 1–53. http://dx.doi.org/10.1016/j.pecs.2014.06.001.

Henry, C., & Minier, J.-P. (2018). Colloidal particle resuspension: On the need for refined characterisation of surface roughness. *Journal of Aerosol Science*, *118*, 1–13. http://dx.doi.org/10.1016/j.jaerosci.2018.01.005.

Henry, C., Minier, J.-P., & Lefèvre, G. (2012). Numerical study on the adhesion and reentrainment of nondeformable particles on surfaces: The role of surface roughness and electrostatic forces. *Langmuir*, *28*, 438–452. http://dx.doi.org/10.1021/la203659q.

Hinds, W. C. (1999). *Aerosol technology : properties, behavior, and measurement of airborne particles* (2nd ed.). New York (N.Y.): Wiley.

Ibrahim, A., Dunn, P., & Brach, R. (2003). Microparticle detachment from surfaces exposed to turbulent air flow: controlled experiments and modeling. *Journal of Aerosol Science*, *34*, 765–782. http://dx.doi.org/10.1016/S0021-8502(03)00031-4.

Ibrahim, A., Dunn, P., & Qazi, M. (2008). Experiments and validation of a model for microparticle detachment from a surface by turbulent air flow. *Journal of Aerosol Science*, *39*, 645–656. http://dx.doi.org/10.1016/j.jaerosci.2008.03.006.

Ilse, K., Khan, M. Z., Lange, K., Gurumoorthy, H. N., Naumann, V., Hagendorf, C., & Bagdahn, J. (2020). Rotational force test method for determination of particle adhesion—from a simplified model to realistic dusts. *Journal of Renewable and Sustainable Energy*, *12*, Article 043503. http://dx.doi.org/10.1063/5.0015122.

Ilse, K., Khan, M. Z., Voicu, N., Naumann, V., Hagendorf, C., & Bagdahn, J. (2019). Advanced performance testing of anti-soiling coatings – Part I: Sequential laboratory test methodology covering the physics of natural soiling processes. *Solar Energy Materials and Solar Cells*, *202*, Article 110048. http://dx.doi.org/10.1016/j.solmat.2019.110048.

Israelachvili, J. N. (2011). *Academic Press*, *Intermolecular and surface forces*. Elsevier.

Jacobs, T. D. B., Ryan, K. E., Keating, P. L., Grierson, D. S., Lefever, J. A., Turner, K. T., Harrison, J. A., & Carpick, R. W. (2013). The effect of atomic-scale roughness on the adhesion of nanoscale asperities: A combined simulation and experimental investigation. *Tribology Letters*, *50*, 81–93. http://dx.doi.org/10.1007/s11249-012-0097-3.

Jiang, X.-L., & Boulos, M. (2006). Induction plasma spheroidization of tungsten and molybdenum powders. *Transactions of the Nonferrous Metals Society of China*, *16*, 13–17. http://dx.doi.org/10.1016/S1003-6326(06)60003-4.

Jiang, Y., Matsusaka, S., Masuda, H., & Qian, Y. (2008). Characterizing the effect of substrate surface roughness on particle wall interaction with the airflow method. *Powder Technology*, *186*, 199–205. http://dx.doi.org/10.1016/j.powtec.2007.11.041.

Johnson, K. L., Kendall, K., & Roberts, A. D. (1971). Surface energy and the contact of elastic solids. *Proceedings of the Royal Society A: Mathematical, Physical and Engineering Sciences*, *324*, 301–313.

Jones, T. B. (1995). *Electromechanics of particles*. Cambridge Univ. Press: OCLC: 31291292.

Kim, Y., Wellum, G., Mello, K., Strawhecker, K. E., Thoms, R., Giaya, A., & Wyslouzil, B. E. (2016). Effects of relative humidity and particle and surface properties on particle resuspension rates. *Aerosol Science and Technology*, *50*, 339–352. http://dx.doi.org/10.1080/02786826.2016.1152350.

Kim, Y.-h., Yiacoumi, S., Lee, I., McFarlane, J., & Tsouris, C. (2014). Influence of radioactivity on surface charging and aggregation kinetics of particles in the atmosphere. *Environmental Science and Technology*, *48*, 182–189. http://dx.doi.org/10.1021/es4047439.

Kottapalli, K., & Novosselov, I. V. (2019). Experimental study of aerodynamic resuspension of RDX residue. *Aerosol Science and Technology*, *53*, 549–561. http://dx.doi.org/10.1080/02786826.2019.1587377.

Kottapalli, K., & Novosselov, I. V. (2021). Aerodynamic resuspension and contact removal of energetic particles from smooth, rough, and fibrous surfaces. *Talanta*, *231*, Article 122356. http://dx.doi.org/10.1016/j.talanta.2021.122356.

Krasheninnikov, S. I., Smirnov, R. D., & Rudakov, D. L. (2011). Dust in magnetic fusion devices. *Plasma Physics and Controlled Fusion*, *53*, Article 083001. http://dx.doi.org/10.1088/0741-3335/53/8/083001.

Kumar, A., Staedler, T., & Jiang, X. (2013). Role of relative size of asperities and adhering particles on the adhesion force. *Journal of Colloid and Interface Science*, *409*, 211–218. http://dx.doi.org/10.1016/j.jcis.2013.07.039.

Kweon, H., Yiacoumi, S., Lee, I., McFarlane, J., & Tsouris, C. (2013). Influence of surface potential on the adhesive force of radioactive gold surfaces. *Langmuir*, *29*, 11876–11883. http://dx.doi.org/10.1021/la4008476.

Kweon, H., Yiacoumi, S., & Tsouris, C. (2015). The role of electrostatic charge in the adhesion of spherical particles onto planar surfaces in atmospheric systems. *Colloids and Surfaces A: Physicochemical and Engineering Aspects*, *481*, 583–590. http://dx.doi.org/10.1016/j.colsurfa.2015.06.030.

Liu, C.-N., Chien, C.-L., Lo, C.-C., Lin, G.-Y., Chen, S.-C., & Tsai, C.-J. (2011). Drag coefficient of a spherical particle attached on the flat surface. *Aerosol and Air Quality Research*, *11*, 482–486. http://dx.doi.org/10.4209/aaqr.2011.05.0069.

Masuda, H., Gotoh, K., Fukada, H., & Banba, Y. (1994). The removal of particles from flat surfaces using a high-speed air jet. *Advanced Powder Technology*, *5*, 205–217.

Matsusaka, S., Wei, D., Yasuda, M., & Sasabe, S. (2015). Adhesive strength distribution of charged particles on metal substrate in external electric field. *Advanced Powder Technology*, *26*, 149–155. http://dx.doi.org/10.1016/j.apt.2014.08.017.

Matsuyama, T., & Yamamoto, H. (1998). The electrostatic force between a charged dielectric particle and a conducting plane. *KONA Powder and Particle Journal*, *16*, 223–228. http://dx.doi.org/10.14356/kona.1998025.

Maugis, D. (1992). Adhesion of spheres: The JKR-DMT transition using a dugdale model. *Journal of Colloid and Interface Science*, *150*, 243–269. http://dx.doi.org/10.1016/0021-9797(92)90285-T.

Mikellides, I., Chen, N., Liao, S., Droz, E., Strimbu, Z., Stricker, M., Chen, F., Malli Mohan, G. B., Anderson, M., Mennella, J., Bernard, D., & Steltzner, A. (2020). Experiments in particle resuspension and transport for the assessment of terrestrial-borne biological contamination of the samples on the mars 2020 mission. *Planetary and Space Science*, *181*, Article 104793. http://dx.doi.org/10.1016/j.pss.2019.104793.

Mohnen, V. A. (1976). Formation, nature, and mobility of ions of atmospheric importance. In H. Dolezalek, R. Reiter, & H. E. Landsberg (Eds.), *Electrical processes in atmospheres* (pp. 1–17). Heidelberg: Steinkopff, http://dx.doi.org/10.1007/978-3-642-85294-7_1.

Mollinger, A. M., & Nieuwstadt, F. T. M. (1996). Measurement of the lift force on a particle fixed to the wall in the viscous sublayer of a fully developed turbulent boundary layer. *Journal of Fluid Mechanics*, *316*, 285–306. http://dx.doi.org/10.1017/S0022112096000547.

O'Neill, M. (1968). A sphere in contact with a plane wall in a slow linear shear flow. *Chemical Engineering Science*, *23*, 1293–1298. http://dx.doi.org/10.1016/0009-2509(68)89039-6.

Otani, Y., Namiki, N., & Emi, H. (1995). Removal of fine particles from smooth flat surfaces by consecutive pulse air jets. *Aerosol Science and Technology*, *23*, 665–673. http://dx.doi.org/10.1080/02786829508965346.

Parsegian, V. A. (2005). *Van Der Waals forces: A handbook for biologists, chemists, engineers, and physicists*. Cambridge: Cambridge University Press, http://dx.doi.org/10.1017/CBO9780511614606.

Pecault, I. T., Gensdarmes, F., Basso, G., & Sommer, F. (2012). Performance assessment of probes dedicated to the monitoring of surface particle contamination. *Particle & Particle Systems Characterization*, *29*, 156–166. http://dx.doi.org/10.1002/ppsc.201200005.

Peillon, S., Autricque, A., Redolfi, M., Stancu, C., Gensdarmes, F., Grisolia, C., & Pluchery, O. (2019). Adhesion of tungsten particles on rough tungsten surfaces using atomic force microscopy. *Journal of Aerosol Science*, *137*, Article 105431. http://dx.doi.org/10.1016/j.jaerosci.2019.105431.

Peillon, S., Dougniaux, G., Payet, M., Bernard, E., Pieters, G., Feuillastre Ressources, S., Garcia-Argote, S., Gensdarmes, F., Arnas, C., Miserque, F., Herlin-Boime, N., Grisolia, C., & Pluchery, O. (2020). Dust sampling in WEST and tritium retention in tokamak-relevant tungsten particles. *Nuclear Materials and Energy*, Article 100781. http://dx.doi.org/10.1016/j.nme.2020.100781.

Petean, P., & Aguiar, M. (2015). Determining the adhesion force between particles and rough surfaces. *Powder Technology*, *274*, 67–76. http://dx.doi.org/10.1016/j.powtec.2014.12.047.

Prokopovich, P., & Starov, V. (2011). Adhesion models: From single to multiple asperity contacts. *Advances in Colloid and Interface Science*, *168*, 210–222. http://dx.doi.org/10.1016/j.cis.2011.03.004.

Rabinovich, Y. I., Adler, J. J., Ata, A., Singh, R. K., & Moudgil, B. M. (2000). Adhesion between Nanoscale Rough Surfaces : measurements and comparison with theory. *Journal of Colloid and Interface Science*, *232*, 17–24. http://dx.doi.org/10.1006/jcis.2000.7168.

Rabinovich, Y. I., Adler, J. J., Ata, A., Singh, R. K., & Moudgil, B. M. (2000). Adhesion between nanoscale rough surfaces : Role of asperity geometry. *Journal of Colloid and Interface Science*, *232*, 10–16. http://dx.doi.org/10.1006/jcis.2000.7167.

Rajupet, S., Riet, A. A., Chen, Q., Sow, M., & Lacks, D. J. (2021). Relative importance of electrostatic and van der Waals forces in particle adhesion to rough conducting surfaces. *Physical Review E*, *103*, Article 042906. http://dx.doi.org/10.1103/PhysRevE.103.042906.

Reeks, M. W., & Hall, D. (2001). Kinetic models for particle resuspension in turbulent flows: theory and measurement. *Aerosol Science*, 1–31.

Rondeau, A., Peillon, S., Vidales, A. M., Benito, J., nac, R. U., Sabroux, J.-C., & Gensdarmes, F. (2021). Evidence of inter-particles collision effect in airflow resuspension of poly-dispersed non-spherical tungsten particles in monolayer deposits. *Journal of Aerosol Science*, *154*, Article 105735. http://dx.doi.org/10.1016/j.jaerosci.2020.105735.

Rubel, M., Widdowson, A., Grzonka, J., Fortuna-Zalesna, E., Moon, S., Petersson, P., Ashikawa, N., Asakura, N., Hamaguchi, D., Hatano, Y., Isobe, K., Masuzaki, S., Kurotaki, H., Oya, Y., Oyaidzu, M., & Tokitani, M. (2018). Dust generation in tokamaks: Overview of beryllium and tungsten dust characterisation in JET with the ITER-like wall. *Fusion Engineering and Design*, *136*, 579–586. http://dx.doi.org/10.1016/j.fusengdes.2018.03.027.

Sarver, T., Al-Qaraghuli, A., & Kazmerski, L. L. (2013). A comprehensive review of the impact of dust on the use of solar energy: History, investigations, results, literature, and mitigation approaches. *Renewable and Sustainable Energy Reviews*, *22*, 698–733. http://dx.doi.org/10.1016/j.rser.2012.12.065.

Sharpe, J. P., & Petti, D. A. (2002). A review of dust in fusion devices: Implications for safety and operational performance. *Fusion Engineering and Design*, *63–64*, 153–163.

Skinner, C. H., Gentile, C. A., Ciebiera, L., & Langish, S. (2004). Tritiated dust levitation by beta-induced static charge. *Fusion Science and Technology*, *45*, 11–14. http://dx.doi.org/10.13182/FST04-A420.

Soltani, M., & Ahmadi, G. (1994). On particle adhesion and removal mechanisms in turbulent flows. *Journal of Adhesion Science and Technology*, *8*, 763–785. http://dx.doi.org/10.1163/156856194X00799.

Sun, Q., Peng, W., & Hai, X. (2021). Mathematical model and atomic force microscopy measurements of adhesion between graphite particles and rough walls. *Applications of Surface Science*, *562*, Article 149976. http://dx.doi.org/10.1016/j.apsusc.2021.149976.

Tabor, D. (1977). Surface forces and surface interactions. *Journal of Colloid and Interface Science*, *58*, 2–13. http://dx.doi.org/10.1016/0021-9797(77)90366-6.

Takeuchi, M. (2006). Adhesion forces of charged particles. *Chemical Engineering Science*, *61*, 2279–2289. http://dx.doi.org/10.1016/j.ces.2004.06.051.

Taylor, N., & Cortes, P. (2014). Lessons learnt from ITER safety & licensing for DEMO and future nuclear fusion facilities. *Fusion Engineering and Design*, *89*, 1995–2000. http://dx.doi.org/10.1016/j.fusengdes.2013.12.030.

Techaumnat, B., & Kadonaga, M. (2011). Electrostatic force behavior of a nonuniformly charged particle on a planar dielectric solid. *IEEE Transactions on Dielectrics and Electrical Insulation*, *18*, 1366–1373. http://dx.doi.org/10.1109/TDEI.2011.6032804.

Tolias, P. (2018). Lifshitz calculations of Hamaker constants for fusion relevant materials. *Fusion Engineering and Design*, *133*, 110–116. http://dx.doi.org/10.1016/j.fusengdes.2018.06.002.

Tolias, P., Ratynskaia, S., De Angeli, M., De Temmerman, G., Ripamonti, D., Riva, G., Bykov, I., Shalpegin, A., Vignitchouk, L., Brochard, F., Bystrov, K., Bardin, S., & Litnovsky, A. (2016). Dust remobilization in fusion plasmas under steady state conditions. *Plasma Physics and Controlled Fusion*, *58*, Article 025009. http://dx.doi.org/10.1088/0741-3335/58/2/025009.

Tyson, W., & Miller, W. (1977). Surface free energies of solid metals: Estimation from liquid surface tension measurements. *Surface Science*, *62*, 267–276. http://dx.doi.org/10.1016/0039-6028(77)90442-3.

Villagrán Olivares, M., Benito, J., Unac, R., & Vidales, A. (2022). Kinetic Monte Carlo method applied to micrometric particle detachment mechanisms by aerodynamic forces. *J. Phys.: Condens. Matter.*, *34*(7), Article 074001. http://dx.doi.org/10.1088/1361-648X/ac3690.

Vitos, L., Ruban, A., Skriver, H., & Kollár, J. (1998). The surface energy of metals. *Surface Science*, *411*, 186–202. http://dx.doi.org/10.1016/S0039-6028(98)00363-X.

Walker, M., McFarlane, J., Glasgow, D., Chung, E., Taboada-Serrano, P., Yiacoumi, S., & Tsouris, C. (2010). Influence of radioactivity on surface interaction forces. *Journal of Colloid and Interface Science*, *350*, 595–598. http://dx.doi.org/10.1016/j.jcis.2010.06.042.

Walton, O. R. (2008). Review of adhesion fundamentals for micron-scale particles. *KONA Powder and Particle Journal*, *26*, 129–141. http://dx.doi.org/10.14356/kona.2008012.

Wen, H., & Kasper, G. (1989). On the kinetics of particle reentrainment from surfaces. *Journal of Aerosol Science*, *20*, 483–498. http://dx.doi.org/10.1016/0021-8502(89)90082-7.

Widdowson, A., Ayres, C., Booth, S., Coad, J., Hakola, A., Heinola, K., Ivanova, D., Koivuranta, S., Likonen, J., Mayer, M., & Stamp, M. (2013). Comparison of JET main chamber erosion with dust collected in the divertor. *Journal of Nuclear Materials*, *438*, S827–S832. http://dx.doi.org/10.1016/j.jnucmat.2013.01.179.

Winter, J. (2004). Dust in fusion devices—a multi-faceted problem connecting high- and low-temperature plasma physics. *Plasma Physics and Controlled Fusion*, *46*, B583–B592. http://dx.doi.org/10.1088/0741-3335/46/12b/047.

Yeh, H., Newton, G., Raabe, O., & Boor, D. (1976). Self-charging of 198 Au-labeled monodisperse gold aerosols studied with a miniature electrical mobility spectrometer. *Journal of Aerosol Science*, *7*, 245–253. http://dx.doi.org/10.1016/0021-8502(76)90039-2.

You, S., & Wan, M. P. (2013). Mathematical models for the van der Waals force and capillary force between a rough particle and surface. *Langmuir*, *29*, 9104–9117. http://dx.doi.org/10.1021/la401516m.

You, S., & Wan, M. P. (2014). Modeling and experiments of the adhesion force distribution between particles and a surface. *Langmuir*, *30*, 6808–6818. http://dx.doi.org/10.1021/la500360f.

Zhang, F., Reeks, M., Kissane, M., & Perkins, R. (2013). Resuspension of small particles from multilayer deposits in turbulent boundary layers. *Journal of Aerosol Science*, *66*, 31–61. http://dx.doi.org/10.1016/j.jaerosci.2013.07.009.

Zhou, H., Götzinger, M., & Peukert, W. (2003). The influence of particle charge and roughness on particle substrate adhesion. *Powder Technology*, *135–136*, 82–91. http://dx.doi.org/10.1016/j.powtec.2003.08.007.

Ziskind, G. (2006). Particle resuspension from surfaces - revisited and re-evaluated. *Reviews in Chemical Engineering*, *22*.

Ziskind, G., Fichman, M., & Gutfinger, C. (1997). Adhesion moment model for estimating particle detachment from a surface. *Journal of Aerosol Science*, *28*, 623–634. http://dx.doi.org/10.1016/S0021-8502(96)00460-0.

Ziskind, G., Yarin, L. P., Peles, S., & Gutfinger, C. (2002). Experimental investigation of particle removal from surfaces by pulsed air jets. *Aerosol Science and Technology*, *36*, 652–659. http://dx.doi.org/10.1080/02786820252883883.